

UNCLASSIFIED

AD 295 992

*Reproduced
by the*

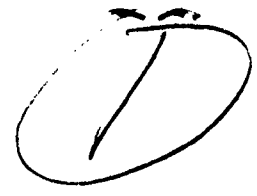
**ARMED SERVICES TECHNICAL INFORMATION AGENCY
ARLINGTON HALL STATION
ARLINGTON 12, VIRGINIA**



UNCLASSIFIED

NOTICE: When government or other drawings, specifications or other data are used for any purpose other than in connection with a definitely related government procurement operation, the U. S. Government thereby incurs no responsibility, nor any obligation whatsoever; and the fact that the Government may have formulated, furnished, or in any way supplied the said drawings, specifications, or other data is not to be regarded by implication or otherwise as in any manner licensing the holder or any other person or corporation, or conveying any rights or permission to manufacture, use or sell any patented invention that may in any way be related thereto.

03-2-3



295 992

295992

AD N
AS

**A CRITICAL STUDY OF
THE DIRECT BLUNT BODY INTEGRAL METHOD**

DECEMBER 28, 1962

DOUGLAS REPORT SM-42603

**MISSILE & SPACE SYSTEMS DIVISION
DOUGLAS AIRCRAFT COMPANY, INC.
SANTA MONICA CALIFORNIA**

48.10

15 12 1962





MISSILE & SPACE SYSTEMS DIVISION
DOUGLAS AIRCRAFT COMPANY, INC
SANTA MONICA, CALIFORNIA

February 8 1963
A2-260-M/AT-AN-5

Subject: Transmittal of Douglas Aircraft Company, Inc., Research Reports SM-42492, SM-42603, and SM-42649

To: Headquarters
Armed Services Technical Information Agency
Air Force Systems Command
United States Air Force
Arlington Hall Station
Arlington 12, Virginia

Attention: TIPA
Joseph Biel
Chief, Accessions Branch
Document Processing Division

1. It is requested that the following unclassified reports be listed on any appropriate publication lists or indexes distributed by ASTIA, such as the Technical Abstract Bulletin. Distribution of these reports to any interested persons or organizations is desired.

Shanahan, R. J., and G. R. Inger. Nonequilibrium Centered Expansion of a Dissociated Supersonic Gas Flow. SM-42492, October 26, 1962.

Xerikos, J., and W. A. Anderson. A Critical Study of the Direct Blunt Body Integral Method. SM-42603, December 28, 1962.

Ormsbee, A. I. Pressure Distribution on a Wedge Accelerated Impulsively at a Supersonic Mach Number. SM-42649, December 28, 1962.

2. Permission is hereby granted to ASTIA to forward these reports to the Office of Technical Services for the printing and sale of copies provided they are reproduced in their entirety and the Douglas Aircraft Company, Inc., designations are retained.

MISSILE & SPACE SYSTEMS DIVISION
Douglas Aircraft Company, Inc.


H. T. Ponsford
H. T. Ponsford, Chief Engineer
Advance Missile Technology

HK:mas
Enclosures as noted
cc: (w/o enclosures)
AF Plant Representative, RWKAC, A

**A CRITICAL STUDY
OF THE DIRECT BLUNT BODY INTEGRAL METHOD**

**DECEMBER 28, 1962
DOUGLAS REPORT SM-42603**

Approved by:



**J.W. Hinde
Chief, Missile Aero/Thermodynamics Section**

Prepared by:
J. Xerikos
Specialist-Gasdynamics Research
W.A. Anderson
Member Of Applied Research Group
Missile Aero/Thermodynamics Section

**PREPARED UNDER THE SPONSORSHIP OF THE
DOUGLAS AIRCRAFT COMPANY INDEPENDENT
RESEARCH AND DEVELOPMENT PROGRAM
ACCOUNT NUMBER 82160-176**

**MISSILE SYSTEMS ENGINEERING | MISSILE & SPACE SYSTEMS DIVISION
DOUGLAS AIRCRAFT COMPANY, INC.**



ABSTRACT

A representative formulation of the one strip blunt body integral method is treated in sufficient detail to delineate the numerical difficulties involved in its mechanization as well as to identify limitations in its application. While the integration of the governing system of equations for general body shapes comprises a two-point boundary value problem, the particular case of a flat-faced cylinder is shown to reduce to a procedure involving a single integration. An investigation is made of the extent to which conservation laws are satisfied throughout the shock layer region. Significant deviations are found to exist depending upon the method used for computing the distribution of flow properties across the shock layer. A procedure has been chosen which insures compatible tangential and normal flow property gradients at the shock and body while significantly reducing mass and momentum defects in most instances. Computed flow field data are presented for spheres and flat-faced cylinders.




TABLE OF CONTENTS

Section		Page
	Abstract	111
	Nomenclature	ix
1.	Introduction	1
2.	Development of Equations	2
3.	Integration Procedure	11
3.1	Integration Scheme: $d\psi/ds$ Continuous at $s=s^*$. . .	13
3.2	Integration Scheme: $d\psi/ds$ Discontinuous at $s=s^*$. .	13
3.3	Initial Values	14
3.3.1	Axisymmetric Case	14
3.3.2	Two-Dimensional Case - Smooth Bodies	15
4.	Convergence Scheme	16
4.1	Initial Value Sensitivity Study	16
4.2	Program Degrees of Freedom	25
5.	Convergence Scheme - Bodies With Sonic Corner	35
6.	Inverse Procedure	36
6.1	Iterative Method	36
6.2	"Linear" Method	37
6.3	Gradient Method	38
7.	Conservation Relations	40

TABLE OF CONTENTS

Section		Page
7.1	Sphere Results	42
7.2	Flat-Faced Cylinder Results	42
8.	Applications	47
8.1	Sphere	47
8.2	Flat-Faced Cylinder	51
8.3	Nose Caps	58
8.4	Two-Dimensional Results	58
9.	Concluding Remarks	63
	References	64
	Appendix A	66
	Appendix B	74

LIST OF FIGURES

Figure		Page
1	$\{S, N\}$ Coordinate System	3
2	Definition of Geometric Variables	5
3	Effect of Convex Corner	12
4	Zone of Influence of Body Curvature Discontinuity	12
5	ϵ Sensitivity Study: $du_0/d\epsilon$ Versus S	18
6	ϵ Sensitivity Study: N Versus S	19
7	ϵ Sensitivity Study: D Versus S	20
8	ϵ Versus N^*	21
9	ϵ Versus S^*	22
10	Halving Mode	24
11	F_i Versus S for $\epsilon = \bar{\epsilon}$	26
12	ϵ Versus N^* : S_p Fixed and Variable	28
13	N^* Versus $\epsilon - \bar{\epsilon}$	29
14	Effect of Fit Distance on $\bar{\epsilon}$	30
15	Effect of Fit Distance on S^*	31
16	Effect of Fit Distance on Downstream Values	32
17	Control Volume	41
18	Shock Layer Mass Balance: Sphere	43
19	Shock Layer Momentum Balance: Sphere	44

LIST OF FIGURES

Figure		Page
20	Shock Layer Mass and Momentum Balance: Flat-Faced Cylinder	45
21	Shock Detachment Distance: Sphere ($\gamma = 1.4$)	48
22	Sonic Point Location: Sphere ($\gamma = 1.4$)	49
23	Shock Wave Curvature at Axis of Symmetry	50
24	Shock Layer Pressure Distribution: Gradient Method	52
25	Shock Layer Density Distribution: Gradient Method	53
26	Shock Layer Mach Number Distribution: Gradient Method	54
27	Comparison of Shock Shapes Derived From Characteristics and Integral Methods	55
28	Surface Pressure and Velocity Distributions for Complete and Truncated Spheres	59
29	Shock Shapes: Flat-Faced Plate and Cylinder	60
30	Pressure and Velocity Distributions: Flat-Faced Plate and Cylinder	61
A1	Definition of Geometric Parameters	67
A2	Stream Tube Geometry	71
B1	Sonic Behavior of Velocity Gradient Expressions	74
B2	Comparison of Exact and L'Hospital Values for dV/ds	76
B3	Sensitivity Study: dV/ds Versus γ	79
B4	Sensitivity Study: dD/ds Versus γ	80

NOMENCLATURE

Symbol

a	Speed of sound
h	Enthalpy
k	$(\gamma-1)/2\gamma$
M	Mach number
p	Pressure
R	Body radius of curvature
R_s	Shock radius of curvature
R	Gas constant
$\bar{r}, \bar{\theta}$	Polar coordinates
s, n	Body oriented curvilinear coordinates
S	Entropy
u	Velocity component
V	Total velocity
x, r	Cylindrical coordinates
γ	Ratio of specific heats, c_p/c_v
δ	Distance from body to shock measured normal to body surface
ϵ	Shock detachment distance at axis of symmetry
θ	Angle between tangent to body and axis of symmetry
θ_s	Angle between tangent to streamline and axis of symmetry

NOMENCLATURE

Symbol

μ	Mach angle, $\sin^{-1} \frac{1}{M}$
ρ	Density
φ	ρ/ρ^*
χ	Angle between tangent to shock and vertical axis
ψ	Stream function

Subscripts

s	Denotes component in s direction
n	Denotes component in n direction
x	Denotes component in x direction
o	Quantity evaluated on body surface
δ	Quantity evaluated on shock wave
∞	Free stream value
t	Stagnation value

The remaining symbols and subscripts are defined in the text.

1. INTRODUCTION

The Dorodnitsyn integral method and its specific applications to mixed flow problems are well represented in the literature, e.g., Refs. 1 through 7. Owing to the nonlinear nature of the two-point boundary value problem involved, however, mechanization of the method involves computing problems of a nonroutine nature. The present report discusses these problems in detail as they arise in the (Belotserkovskii) one strip approximation. Further results concerning the basic techniques involved as well as applications to blunt-nosed configurations are presented. Particular attention is paid to the determination of flow properties across the shock layer. For the sake of completeness the development of equations is presented in detail. The procedure and attendant notation largely follow Ref. 5.

2. DEVELOPMENT OF EQUATIONS

The equations expressing conservation of mass, momentum and energy for a perfect, inviscid, non-heat conducting gas are, respectively,

$$\nabla \cdot \rho \vec{V} = 0 \quad (2-1)$$

$$(\nabla \times \vec{V}) \times \vec{V} + \frac{1}{2} \nabla V^2 + \frac{1}{\rho} \nabla \epsilon p = 0 \quad (2-2)$$

$$\nabla \cdot \nabla \left(\frac{p}{\rho \epsilon} \right) = 0, \quad (2-3)$$

where $\epsilon = \frac{\gamma-1}{2\gamma} = \frac{a_\infty^2}{\gamma V_{max}^2}, \quad a^2 = \frac{k\gamma p}{\rho}$

Velocity, pressure and density have been nondimensionalized through use of maximum velocity and free stream stagnation pressure and density. This choice of parameters has particular advantage when applied to the Bernoulli equation.

For general, curvilinear orthogonal coordinates (x_1, x_2, x_3) where $(ds)^2 = h_1^2(dx_1)^2 + h_2^2(dx_2)^2 + h_3^2(dx_3)^2$ and $V = \vec{i}u + \vec{j}v + \vec{k}w$, the vector operations are given by

$$\nabla \cdot \vec{V} = \frac{1}{h_1 h_2 h_3} \left[\frac{\partial}{\partial x_1} (h_2 h_3 u) + \frac{\partial}{\partial x_2} (h_3 h_1 v) + \frac{\partial}{\partial x_3} (h_1 h_2 w) \right]$$

$$\nabla V = \vec{i} \frac{1}{h_1} \frac{\partial V}{\partial x_1} + \vec{j} \frac{1}{h_2} \frac{\partial V}{\partial x_2} + \vec{k} \frac{1}{h_3} \frac{\partial V}{\partial x_3}$$

$$\nabla \times \vec{V} = \vec{e}_1 \frac{1}{h_2 h_3} \left[\frac{\partial}{\partial x_2} (h_3 v_3) - \frac{\partial}{\partial x_3} (h_2 v_2) \right] + \vec{e}_2 \frac{1}{h_3 h_1} \left[\frac{\partial}{\partial x_3} (h_1 v_1) - \frac{\partial}{\partial x_1} (h_3 v_3) \right] + \vec{e}_3 \frac{1}{h_1 h_2} \left[\frac{\partial}{\partial x_1} (h_2 v_2) - \frac{\partial}{\partial x_2} (h_1 v_1) \right]$$

Since only axisymmetric and two-dimensional configurations will be treated, a body-oriented curvilinear coordinate system (Fig. 1) is defined such that

$$h_1 = 1 + \frac{R^2}{R} = 1 - r \frac{d\theta}{ds}$$

$$h_2 = 1$$

$$h_3 = r \begin{cases} j=0 & \text{two-dimensional case} \\ j=1 & \text{axisymmetric case} \end{cases}$$

$$x_1 = s, \quad \frac{\partial}{\partial x_3} \equiv 0$$

$$x_2 = r, \quad v_3 \equiv 0$$

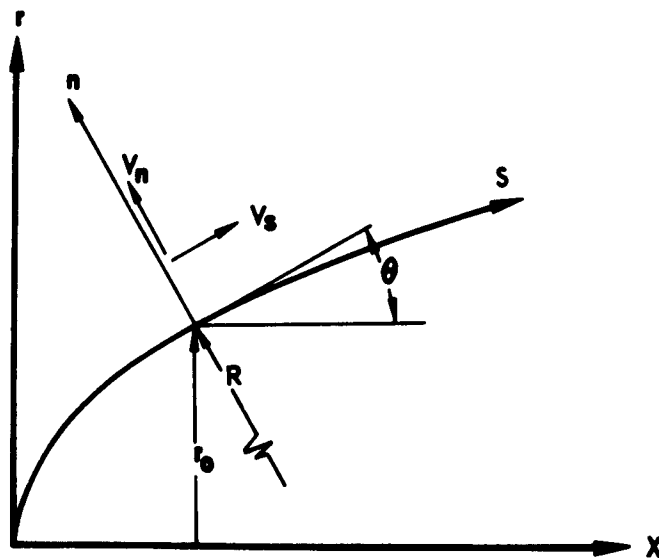


FIGURE 1

Substituting the Bernoulli equation for the momentum equation in the s -direction, the governing system of equations becomes

$$\frac{\partial}{\partial s}(\rho \psi r') + \frac{\partial}{\partial n} \left[\left(1 + \frac{n}{R}\right) \rho \psi_n r' \right] = 0 \quad (2-4)$$

$$\psi \frac{\partial \psi_n}{\partial s} + \left(1 + \frac{n}{R}\right) \psi_n \frac{\partial \psi_n}{\partial n} - \frac{\psi_s^2}{R} + \frac{k}{\rho} \left(1 + \frac{n}{R}\right) \frac{\partial \rho}{\partial n} = 0 \quad (2-5)$$

$$\frac{\rho}{\rho_0} = \varphi(\psi) \quad (2-6)$$

$$V^2 + \frac{\rho}{\rho_0} = 1 \quad (2-7)$$

$$\text{Let } \tau = \tau \psi_s \quad (a)$$

$$h = \tau \psi_n \quad (b)$$

$$Z = \rho \psi_s \psi_n \quad (c)$$

$$H = \rho \psi_n^2 + k \rho \quad (d) \quad (2-8)$$

$$g = \rho \psi_s^2 + k \rho \quad (e)$$

$$G = \frac{k}{R} g + j \left(1 + \frac{n}{R}\right) \cos \theta k \rho, \quad (f)$$

$$\text{where } \tau = (1 - V^2)^{\frac{1}{\sigma-1}}$$

Using Eqs. (2-6), (2.7) and (2.9), it follows that

$$\rho = \tau \varphi^{\frac{1}{\sigma-1}} \quad (2-10)$$

A modified continuity equation is obtained through use of Eqs. (2-8a), (2-8b), (2-10) and the relation $\nabla \cdot \nabla \phi = 0$:

$$\frac{\partial}{\partial s}(r'Z) + \frac{\partial}{\partial n}[(1 + \frac{\partial}{\partial s})r'h] = 0 \quad (2-11)$$

In addition, Eqs. (2-4) and (2-5) are combined to obtain a modified momentum equation in "divergence" form.*

$$\frac{\partial}{\partial s}(r'Z) + \frac{\partial}{\partial n}[(1 + \frac{\partial}{\partial s})r'h] - G = 0 \quad (2-12)$$

Integrand Approximations

Consider an equation given in divergence form, i.e.,

$$\frac{\partial}{\partial s} I_1(s, n) + \frac{\partial}{\partial n} I_2(s, n) + I_3(s, n) = 0$$

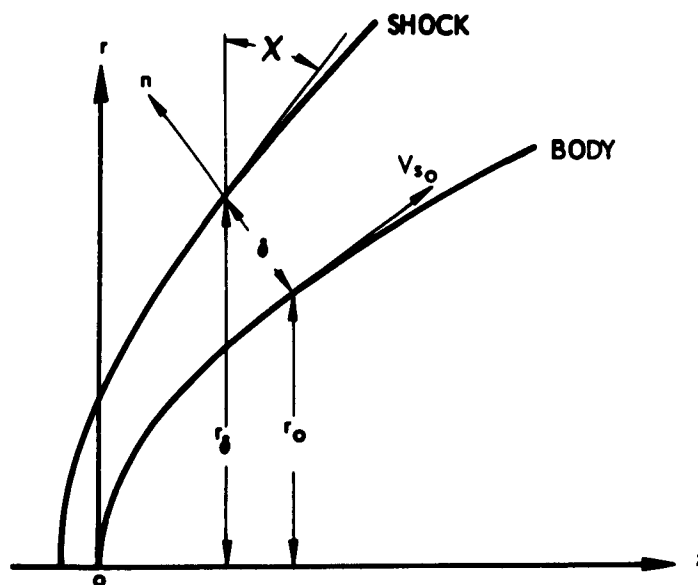


FIGURE 2

* More precisely, one takes $\rho r' \times$ Eq. (2-5) + $\rho h \times$ Eq. (2-4) and adds and subtracts $\frac{\partial}{\partial n}[(1 + \frac{\partial}{\partial s})r'h] - \frac{\partial}{\partial s}Z\rho$.

Integrating along an arbitrary line in the n -direction, e.g., across the shock layer from the body, $n=0$, to the shock, $n=\delta(s)$, (Fig. 2), one obtains

$$\int_0^{\delta} \frac{\partial I_1}{\partial s} dn + \int_0^{\delta} \frac{\partial I_2}{\partial n} dn + \int_0^{\delta} I_3 dn = 0$$

If the functions I_1 , I_3 are approximated in the form

$$I_i = I_{i0}(s) + \frac{n}{\delta} [I_{i\delta}(s) - I_{i0}(s)] \quad ,$$

it follows that

$$\int_0^{\delta} I_i dn = \frac{\delta}{2} (I_{i\delta} + I_{i0})$$

Applying Leibnitz's rule, one obtains an ordinary, first-order differential equation:

$$\frac{d}{ds} \left[\frac{\delta}{2} (I_{1\delta} + I_{10}) \right] - I_{1\delta} \frac{d\delta}{ds} + I_{2\delta} - I_{20} + \frac{\delta}{2} (I_{3\delta} + I_{30}) = 0$$

The integrand approximations employed in the present equations are

$$\left. \begin{aligned} r_z^i &= r_0^i z_0 + \frac{n}{\delta} (r_\delta^i z_\delta - r_0^i z_0) \\ r_z^i &= \frac{n}{\delta} r_\delta^i z_\delta \quad , \quad (z_0 \equiv 0) \\ G &= G_0 + \frac{n}{\delta} (G_\delta - G_0) \end{aligned} \right\} \quad (2-13)$$

The only formal mathematical restriction on the choice of representation is that the right hand side of Eqs. (2-13) be a specified function of η containing \mathcal{S} -dependent parameters which are evaluated at either the shock or body (for the one strip approximation). For example, one may specify

$$r'z = r'[z_0 + \frac{\mathcal{S}}{\mathcal{S}}(z_s - z_0)]$$

or

$$r'z = (\frac{\mathcal{S}}{\mathcal{S}})^2 r'_s z_s$$

In some instances, the specified function of η may lead to behavior in direct contradiction to known inviscid results, e.g., incorrect surface or shock gradients of flow properties. A more complete discussion of the validity of the approximations is given under Inverse Procedures.

Applying the preceding considerations to the modified continuity and momentum equations yields (noting that $h_0 = z_0 = 0$):

$$\frac{1}{2}(r'_0 z_0 - r'_s z_s) \frac{d\mathcal{S}}{d\mathcal{S}} + \frac{\mathcal{S}}{2} \left[\frac{d}{d\mathcal{S}}(r'_s z_s) + \frac{d}{d\mathcal{S}}(r'_0 z_0) \right] + (1 + \frac{\mathcal{S}}{\mathcal{R}}) r'_s h_s = 0 \quad (2-14)$$

$$-\frac{1}{2} r'_s z_s \frac{d\mathcal{S}}{d\mathcal{S}} + \frac{\mathcal{S}}{2} \frac{d}{d\mathcal{S}}(r'_s z_s) + r'_s h_s (1 + \frac{\mathcal{S}}{\mathcal{R}}) - r'_0 h_0$$

(2-15)

$$-\frac{1}{\mathcal{R}} \frac{\mathcal{S}}{2} (r'_s g_s + r'_0 g_0) - j \cos \theta \frac{\mathcal{S}}{2} \left[(1 + \frac{\mathcal{S}}{\mathcal{R}}) p + p_0 \right] = 0$$

Eqs. (2-14) and (2-15) may be expressed entirely in terms of the dependent variables δ , ψ_0 and χ through use of the following auxiliary relationships:

$$r_f^j = r_0^j + j\delta \cos \theta$$

$$\rho_f = (1 - V_f^2)^{\frac{\gamma}{\gamma-1}} \rho_0^{\frac{\gamma}{\gamma-1}}$$

$$\rho_f = (1 - V_f^2)^{\frac{\gamma}{\gamma-1}} \rho_0^{\frac{\gamma}{\gamma-1}}$$

$$\varphi_f = \left[\frac{2\gamma M_\infty^2 \cos^2 \chi - (\gamma-1)}{\gamma+1} \right] \left[\frac{2 + (\gamma-1) M_\infty^2 \cos^2 \chi}{(\gamma+1) M_\infty^2 \cos^2 \chi} \right]^{\frac{\gamma}{\gamma-1}}$$

$$\psi_f = m(\alpha \cos \theta + \beta \sin \theta)$$

$$\psi_f = m(\alpha[-\sin \theta] + \beta \cos \theta)$$

$$m = M_\infty \left[\frac{\gamma-1}{2 + (\gamma-1) M_\infty^2} \right]^{\frac{1}{2}}$$

$$\alpha = 1 - \frac{2}{\gamma+1} (\cos^2 \chi - \frac{1}{M_\infty^2})$$

$$\beta = \frac{2}{\gamma+1} \tan \chi (\cos^2 \chi - \frac{1}{M_\infty^2})$$

oblique
shock
relations

$$\rho_0 = (1 - V_0^2)^{\frac{\gamma}{\gamma-1}} \rho_0^{\frac{\gamma}{\gamma-1}}$$

$$\rho_0 = (1 - V_0^2)^{\frac{\gamma}{\gamma-1}} \rho_0^{\frac{\gamma}{\gamma-1}}$$

$$\varphi_0 = (\varphi_f)_{\chi=0}$$

Expanding Eqs. (2-14) and (2-15) and introducing a geometrical relationship between δ and k , one obtains the governing system of equations in final form:

$$\frac{d\delta}{dS} = \frac{1 + \frac{\delta}{R}}{\tan(\theta + k)} \quad (2-16)$$

$$\frac{dk}{dS} = \frac{F_1 + F_2 \frac{d\delta}{dS}}{F_3} \quad (2-17)$$

$$\frac{d\psi_0}{dS} = \frac{F_4 + F_5 \frac{d\delta}{dS} + F_6 \frac{dk}{dS}}{F_7} = \frac{N}{D} \quad (2-18)$$

where

$$F_1 = -\varphi^{\frac{1}{\delta-1}} (1 - \nu_s^2)^{\frac{\delta-1}{2}} \left[\psi_2^2 (1 + \frac{\delta}{2R}) \nu_s^{\frac{1}{2}} + j \psi_2 \psi_3 (1 + \frac{\delta}{R}) \frac{\delta}{2} \sin \theta \right] \\ + \varphi^{\frac{1}{\delta-1}} (1 - \psi_2^2)^{\frac{\delta-1}{2}} \psi_2^2 \frac{\delta}{2R} \nu_s^{\frac{1}{2}} - \epsilon \left\{ \left[\nu_s^{\frac{1}{2}} (1 + \frac{\delta}{2R}) - j \frac{\delta}{2} \cos \theta (1 + \frac{\delta}{R}) \right] \times \right. \\ \left. (1 - \nu_s^2)^{\frac{\delta-1}{2}} \varphi^{\frac{1}{\delta-1}} - (1 - \psi_2^2)^{\frac{\delta-1}{2}} \varphi^{\frac{1}{\delta-1}} \left[\nu_0^{\frac{1}{2}} (1 + \frac{\delta}{2R}) + j \frac{\delta}{2} \cos \theta \right] \right\}$$

$$F_2 = \frac{\nu_s^{\frac{1}{2}}}{2} (1 - \nu_s^2)^{\frac{\delta-1}{2}} \varphi^{\frac{1}{\delta-1}} \psi_2 \psi_3$$

$$F_3 = \delta \nu_s^{\frac{1}{2}} (1 - \nu_s^2)^{\frac{\delta-1}{2}} \frac{2M}{\delta+1} \left[\psi_2 (1 - \frac{\delta}{2} \psi_2^2) \frac{\delta}{2} + \psi_3 (1 - \frac{\delta}{2} \psi_3^2) \frac{\delta}{2} \right] \varphi^{\frac{1}{\delta-1}} \\ + 2\delta \nu_s^{\frac{1}{2}} (1 - \nu_s^2)^{\frac{\delta-1}{2}} \psi_2 \psi_3 \tan k \left(\frac{\delta}{\delta+1} \right) \left[\frac{(M_0^2 \cos^2 k - 1)^2}{2 + (\gamma-1) M_0^2 \cos^2 k} \right] \left[\frac{2 + (\gamma-1) M_0^2 \cos^2 k}{(\gamma+1) M_0^2 \cos^2 k} \right] \varphi^{\frac{\delta}{\delta-1}}$$

$$F_4 = -\left(1 + \frac{\delta}{2R}\right) \gamma_f (1 - \gamma_f^2)^{\frac{\gamma_f - 1}{2}} \gamma_g - j \frac{\delta}{2} \sin \theta \left[(1 - \gamma_g^2)^{\frac{\gamma_f - 1}{2}} \gamma_g \right. \\ \left. + (1 - \gamma_f^2)^{\frac{\gamma_g - 1}{2}} \gamma_g (1 + \frac{\delta}{R}) \right]$$

$$F_5 = -\frac{\delta}{2} \left[(1 - \gamma_g^2)^{\frac{\gamma_f - 1}{2}} \gamma_g - (1 - \gamma_f^2)^{\frac{\gamma_g - 1}{2}} \gamma_g \right]$$

$$F_6 = -\delta \gamma_f (1 - \gamma_f^2)^{\frac{\gamma_f - 1}{2}} \frac{2\gamma_f}{\gamma_f + 1} \left[(1 - \gamma_g^2)^{\frac{\gamma_f - 1}{2}} \gamma_f - \gamma_g \gamma_g \frac{\gamma_f}{2} \right]$$

$$F_7 = \frac{\delta \gamma_g}{2} (1 - \gamma_g^2)^{\frac{\gamma_g - 1}{2}} \left(1 - \frac{\gamma_f + 1}{\gamma_f - 1} \gamma_g^2 \right)$$

$$\tau_1 = \left[\frac{1}{2} \left(1 - \frac{1}{\gamma_{\infty}^2 \cos^2 \varphi} \right) - \sin^2 \varphi \right] \sin \theta - \sin \varphi \cos \varphi \cos \theta$$

$$\tau_2 = \left[\frac{1}{2} \left(1 - \frac{1}{\gamma_{\infty}^2 \cos^2 \varphi} \right) - \sin^2 \varphi \right] \cos \theta - \sin \varphi \cos \varphi \sin \theta$$

$$\tau_3 = \frac{2}{(\gamma - 1)(1 - \gamma_f^2)}$$

3. INTEGRATION PROCEDURE

In order to initiate the numerical integration of the system of nonlinear total differential equations, knowledge of the dependent variables δ , χ and χ_s at the axis ($s=0$) is required. The initial values $d\chi/ds$ and $d\chi_s/ds$ are indeterminate at the axis and require special treatment. One may deduce immediately that $\chi(0) = \chi_s(0) = 0$; however, the shock detachment distance $\delta(0) = \bar{\epsilon}$ remains unknown and must be determined from an auxiliary condition. A two-point boundary value problem therefore exists which must be solved by means of an iterative approach. (A bar will be used to distinguish the "precise" or final value of $\bar{\epsilon}$ as opposed to an estimated value during iteration.) The specific approach taken depends on nose geometry and its influence on the surface velocity gradient.

A few preliminary remarks are in order before discussing the two types of integration procedures. Application of the integral method to smooth bodies (i.e., having continuous slope) is facilitated by the choice of a natural coordinate system such that the body surface coincides with a coordinate surface. In particular, this choice insures the vanishing of the normal component of the surface velocity which leads to certain analytical simplifications. Employing body-oriented orthogonal curvilinear coordinates, as in the present case, one is only practically limited by the difficulty in analytically describing arc length, radius, slope and curvature along the body surface. However, when a slope discontinuity (convex corner) is encountered, the s -derivatives become infinite at this point and an "area of omission" exists which prevents continuation of the integration. There will be a class of physically meaningful solutions (for the region from the axis to the corner) obtained when the corner corresponds to the body sonic point (Fig. 3).

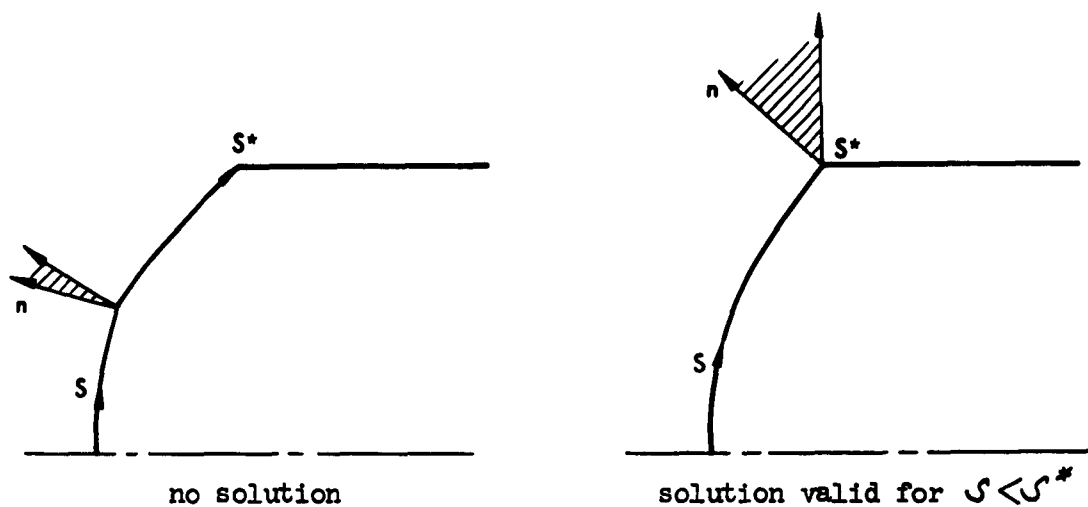


FIGURE 3

A mechanism in the integral method which tends to further limit its applicability in certain cases is the direct transmission of body information to the field immediately normal to the body rather than, for example, along a characteristic direction in the supersonic regime, e.g., Fig. 4.

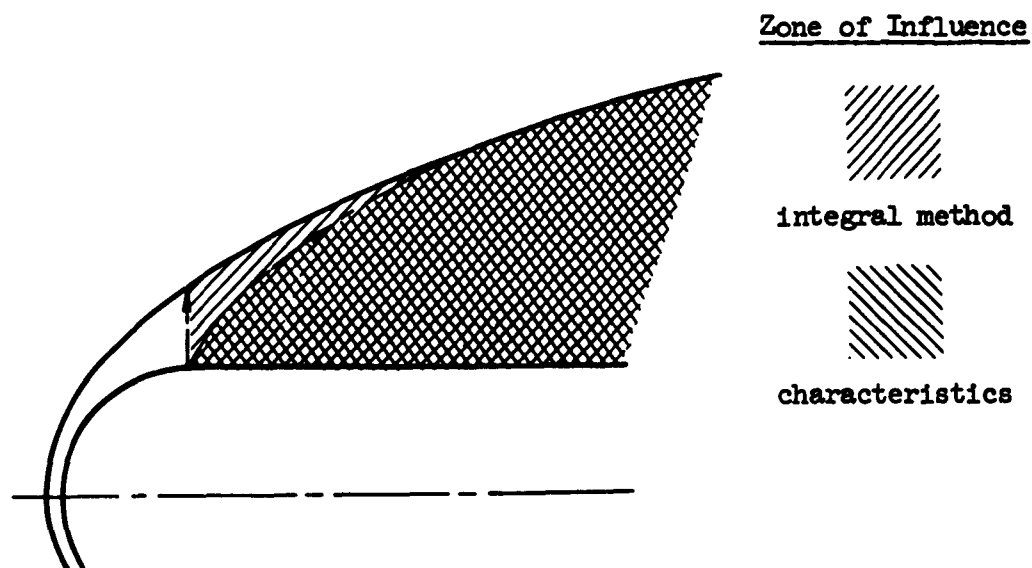


FIGURE 4

Thus a change in body slope or curvature imposes an immediate perturbation across the adjoining field. This effect should be less pronounced in the transonic region where the "normal" mode of information transmittal is more nearly realized in the physical case. It may be reasoned that this effect will be suppressed as the integral approximations are improved through further subdivision of the shock layer. However, by rewriting Eq. (2-16) (which is a geometrical relationship independent of the integral approximations) as

$$\frac{d\delta}{ds} = (1 - \delta \frac{d\theta}{ds}) \cot(\theta + \chi),$$

it can be seen that a curvature discontinuity, e.g., hemisphere-cylinder which involves a change in curvature from unity to zero, results in a discontinuity in $d\delta/ds$ at the same value of s . Further, this discontinuity is introduced into the expressions for $d\chi/ds$ and $d\psi_0/ds$ (which contain $d\delta/ds$). Caution must therefore be exercised in interpreting flow field results in cases involving rapid changes in body geometry.

3.1 Integration Scheme: $d\psi_0/ds$ Continuous at $s = s^*$

Assuming that the body slope is defined by a continuous and monotonically decreasing function, both physical and mathematical reasoning calls for continuity of the surface velocity gradient. The denominator of the expression for $d\psi_0/ds$, however, vanishes identically at the sonic point. The auxiliary condition for determining $\bar{\epsilon}$ therefore becomes

$$N(\bar{\epsilon}, s^*) = 0$$

in order that $\lim_{s \rightarrow s^*} N_D$ be finite. Further justification for this procedure is given in Appendix B.

3.2 Integration Scheme: $d\psi_0/ds$ Discontinuous at $s = s^*$

When the sonic point is known to coincide with a convex corner, a discontinuity in the velocity gradient at this point is consistent with

requirements of inviscid theory. The previous auxiliary condition is therefore no longer valid. One must now vary ϵ until

$$S^* = S_{\text{CORNER}}$$

There is a class of bodies for which a definitive choice of method cannot be made, e.g., sharp-cornered spherical caps. For example, if the sonic point occurs below a convex corner (on a smooth portion of the body), it will not be possible to attain the requirement $S^* = S_{\text{CORNER}}$. Further, if the corner lies below the intersection of the "limiting characteristic"* and the body, the slope discontinuity can in principle still affect the upstream subsonic and transonic flow regions. In practice, however, there is no feedback scheme in the one strip integral method to properly account for this effect.

3.3 Initial Values

3.3.1 Axisymmetric Case

Direct substitution of the initial values into Eqs. (2-16), (2-17) and (2-18) results in indeterminate (0/0) expressions for $(\partial \psi_s / \partial s)_0$ and $(\partial k / \partial s)_0$. Application of L'Hospital's rule yields the proper starting values,

$$\left(\frac{\partial \psi_s}{\partial s} \right)_0 = - \frac{U_{\eta s_0} (1 - U_{\eta s_0}^2)^{\frac{\gamma-1}{2}}}{\epsilon} \left(1 + \frac{\epsilon}{R} \right) \left[1 - \epsilon \left(\frac{\partial k}{\partial s} \right)_0 \frac{2(M_{\infty}^2 - 1)}{2 + (\gamma - 1)M_{\infty}^2} \right]$$

$$\left(\frac{\partial k}{\partial s} \right)_0 = \frac{2 + (\gamma - 1)M_{\infty}^2}{2\epsilon U_{\eta s_0}^2 (M_{\infty}^2 - 1)} \left[U_{\eta s_0}^2 + \epsilon (1 - U_{\eta s_0}^2) - \epsilon (1 - U_{\eta s_0}^2)^{\frac{\gamma-1}{2}} \right],$$

*Ref. 13 defines the limiting characteristic as the "locus of points each of which has only one point of the sonic line in its zone of action."

where
$$\dot{u}_{\delta_0} = - \frac{m[2 + (\gamma-1)M_\infty^2]}{(\gamma+1)M_\infty^2}$$

Also, by symmetry

$$\left(\frac{d\delta}{ds}\right)_0 = 0$$

3.3.2 Two-Dimensional Case

No indeterminateness arises in this case (primarily due to the absence of the radius terms); therefore, no special formulation is required. It is interesting to note the relationship existing between two-dimensional and axisymmetric initial derivatives, i.e.,

$$\left(\frac{d\dot{u}_0}{ds}\right)_{2D} = \frac{2\bar{\epsilon}_{3D}}{\bar{\epsilon}_{2D}} \left(1 + \frac{\bar{\epsilon}_{2D}}{2R}\right) \left(\frac{d\dot{u}_0}{ds}\right)_{3D} \quad (3-1)$$

$$\left(\frac{dK}{ds}\right)_{2D} = \frac{2\bar{\epsilon}_{3D}}{\bar{\epsilon}_{2D}} \left(1 + \frac{\bar{\epsilon}_{2D}}{2R}\right) \left(\frac{dK}{ds}\right)_{3D} \quad (3-2)$$

4. CONVERGENCE SCHEME - SMOOTH BODIES

As indicated earlier, the determination of the correct initial values of $S(0) = \bar{\epsilon}$ involves the expression for the surface velocity gradient which for convenience may be expressed as $\partial \psi_0 / \partial s = N/D$. Assuming that $N(\bar{\epsilon}, S^*(\bar{\epsilon})) = D(S^*(\bar{\epsilon})) = 0$, L'Hospital's rule states that if there exists a neighborhood of $S = S^*$ such that $D(S) \neq 0$ except for $S = S^*$, and $N'(S^*)$ and $D'(S^*)$ exist and do not vanish simultaneously, then $\lim_{S \rightarrow S^*} N/D = \lim_{S \rightarrow S^*} N'/D'$ whenever the limit on the right exists. However, in the present case, for $\epsilon \neq \bar{\epsilon}$, $N(\epsilon, S^*) = N^* \neq 0$ and $\partial \psi_0 / \partial s$ displays singular behavior in the neighborhood of S^* . One must also note that since S^* is a function of ϵ , it is in effect a "floating" singular point.

Basically, the iterative process involves successive refinements of ϵ such that N^* is reduced in magnitude to the extent that the singular behavior of N/D is confined to a small neighborhood of S^* . At this point, extrapolation techniques may be applied with little loss in accuracy in order to continue the integration beyond $S = S^*$.

4.1 Initial Value Sensitivity Study

In order to establish the feasibility of a given prediction-correction scheme, it is necessary to establish the sensitivity of the integration to the choice of ϵ . From the standpoint of physical measurements, it is reasonable to expect that a carefully conducted experiment will yield shock standoff distances (in terms of nose radii) accurate to two significant figures. In the present integral method, for a given M_∞, γ , integrand approximation, etc., there exists a precise value of $\epsilon = \bar{\epsilon}$ (which, rounded off to two or three figures, is physically acceptable) which will cause the solution to be sufficiently well behaved in the sonic region

such that the integration may be continued into the supersonic regime. The degree of precision called for was found to be in excess of eight decimal places.* Figs. 5 through 7 explicitly illustrate the behavior of the most sensitive function involved, i.e., $d\psi_0/ds$, N and D , when ϵ is perturbed plus or minus one digit from a reference value in the second through eighth decimal places. The saddle point nature of the singularity at the sonic point mentioned by previous investigators (e.g., Ref. 6) is clearly evident. Note that for a poor guess of ϵ , the neighborhood for which $d\psi_0/ds$ is significantly affected extends back to the stagnation point, e.g., for $\epsilon - \bar{\epsilon} = \pm .01$, a deviation of approximately six percent in $(d\psi_0/ds)_0$ occurs. It should be emphasized that the figures presented require a knowledge of $\bar{\epsilon}$ and hence represent an "a posteriori" view of the convergence procedure.

Initial attempts to satisfy the downstream sonic condition consisted of a series of "single pass" integrations with a running plot being kept of N^* and S^* in order to make successive predictions of ϵ (Figs. 8 and 9). The stopping conditions were either $N^* \leq 0$ or $\psi_0 > \eta\alpha^*$, $0 < \eta < 1$. Values of N^* and S^* were determined by means of extrapolation polynomials (of degree $f = 2$) applied successively to ψ_0 (to determine S^*) and N [to determine $N^*(S^*)$]. A positive value of N^* indicated that ϵ was too small while a negative value indicated that ϵ was too large. It quickly became apparent that a slope prediction technique alone could not cope with the nonlinear behavior of the functions during early stages of convergence.

A value of standoff distance established for N^* sufficiently small will be biased by choice of the parameters f and η . Therefore, if f or η are to be changed during the iterative process, a high degree of refinement of ϵ is not called for prior to the change. Regarding the parameter,

* This necessitated the use of a double-precision mode of operation (IBM 7090-FORTRAN). Unfortunately, double-precision input and readout capabilities were not available; therefore, the exact number of figures required beyond eight could not be established.

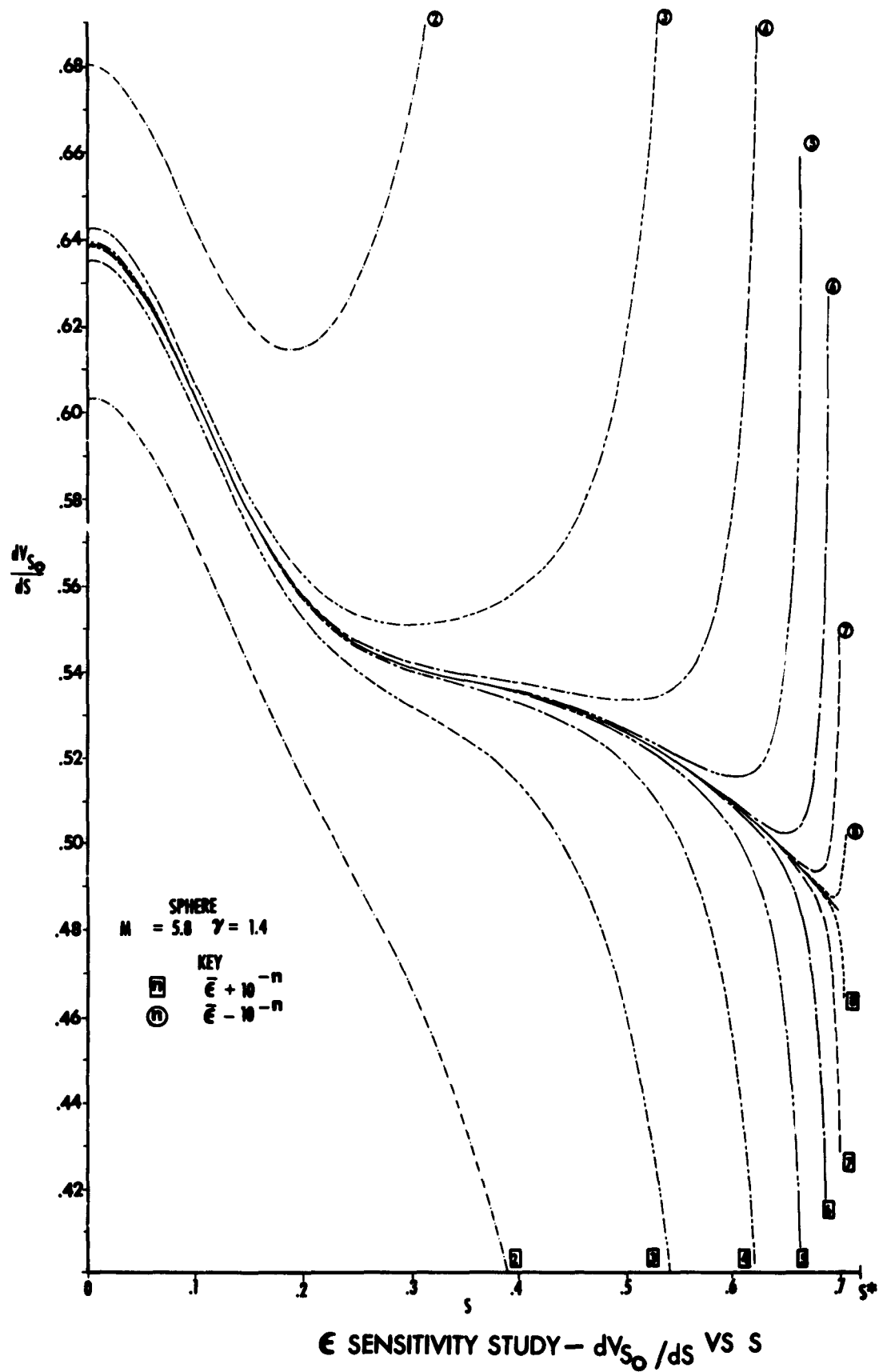


FIGURE 5

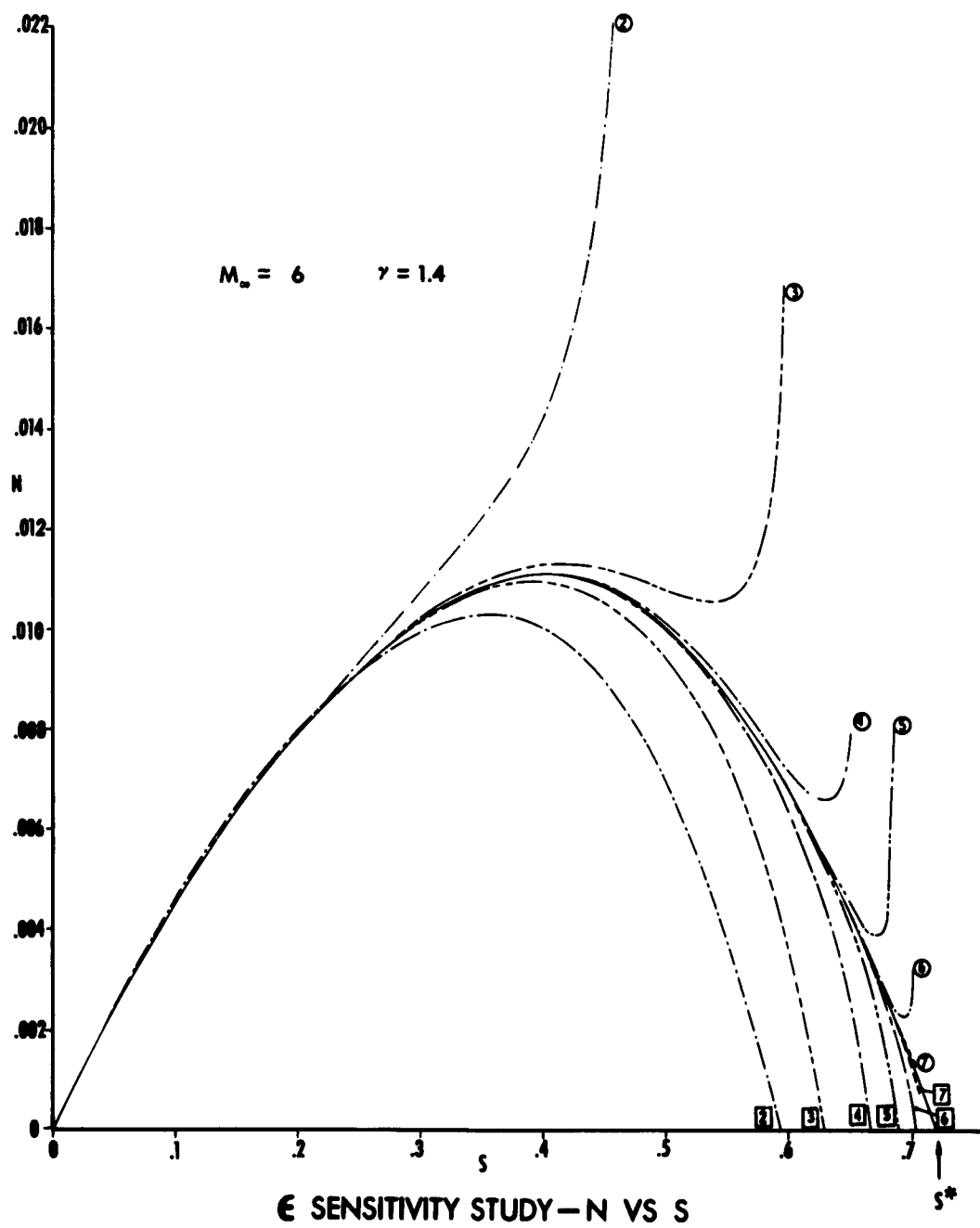


FIGURE 6

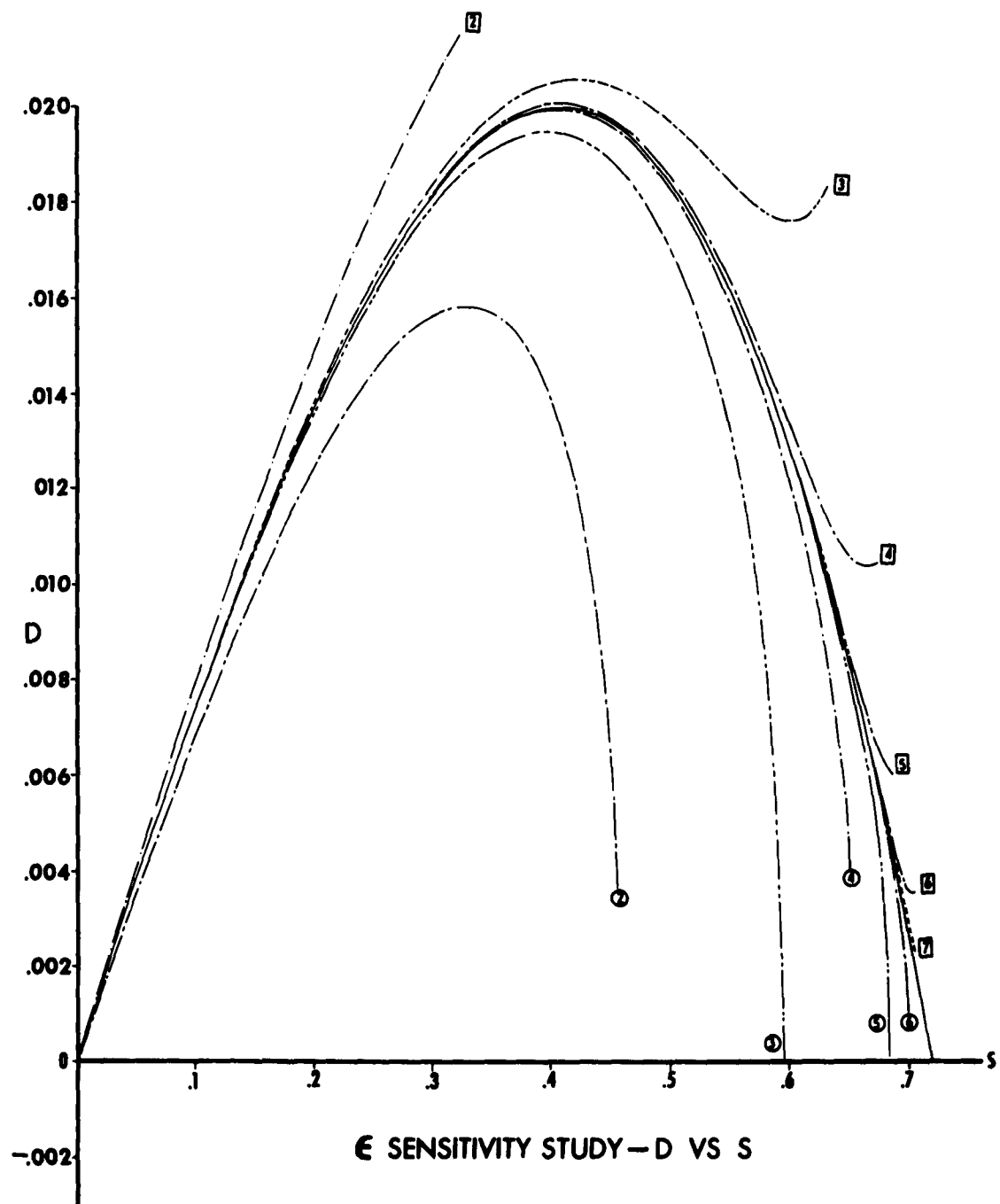


FIGURE 7

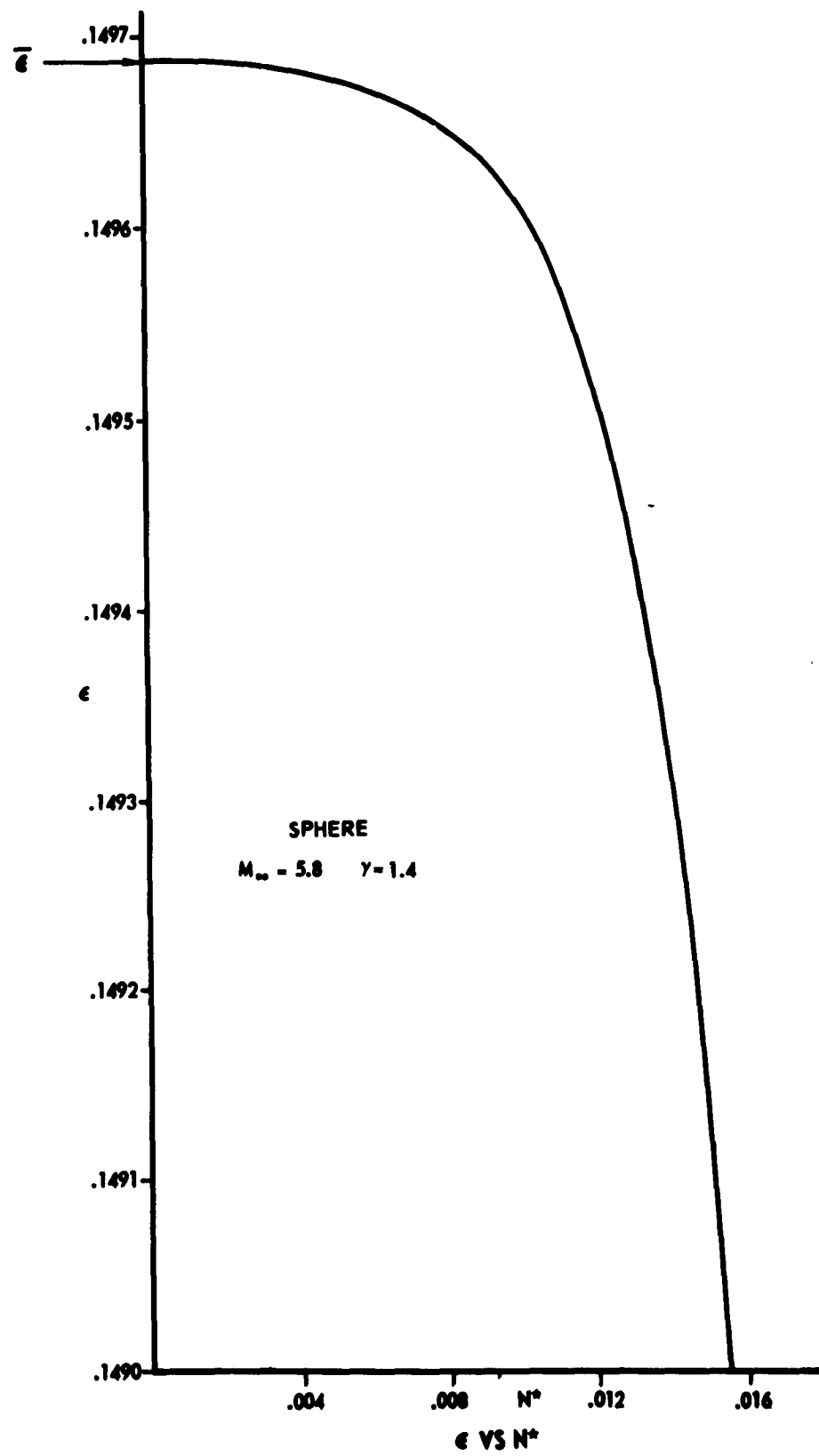


FIGURE 8

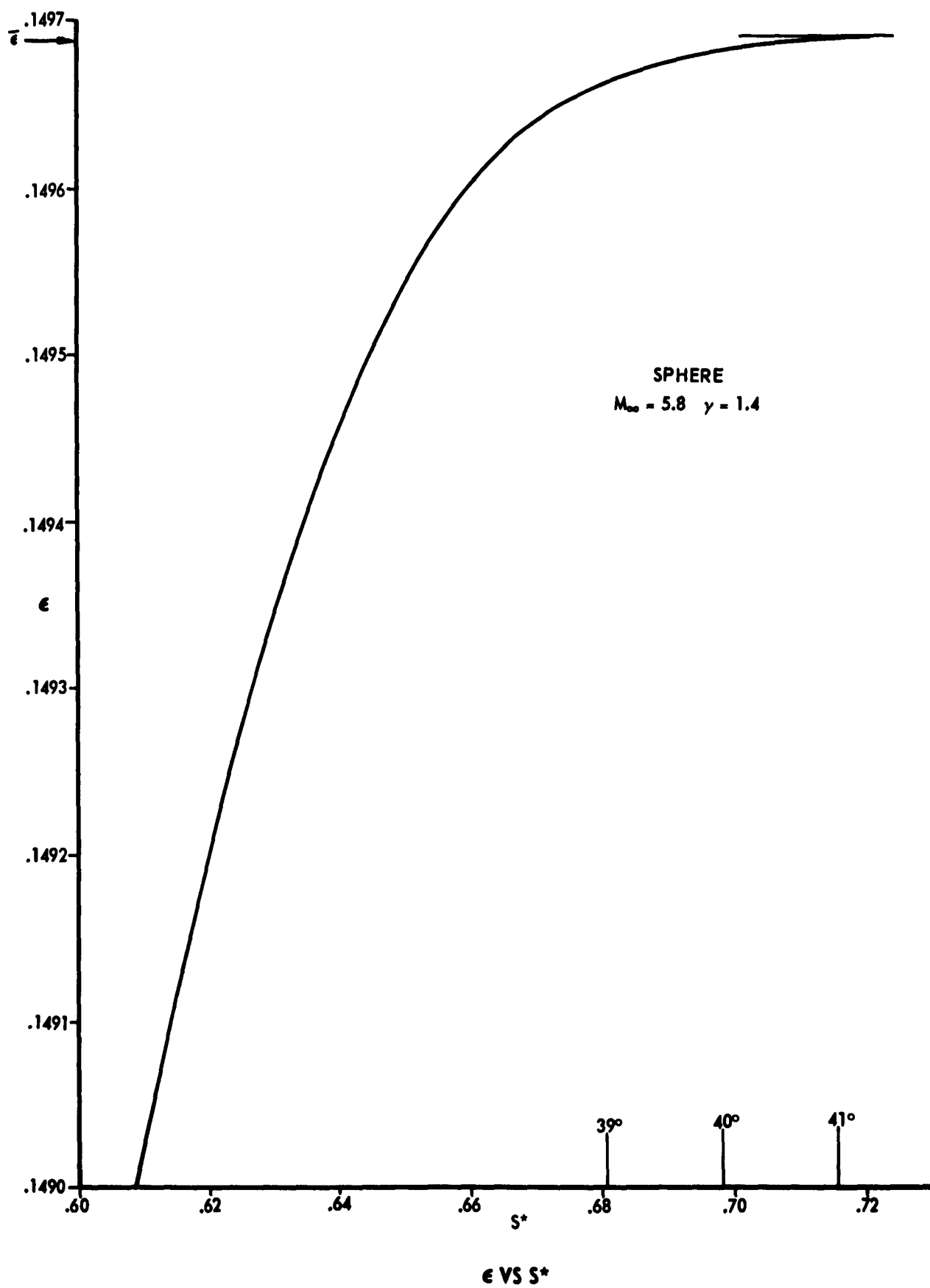


FIGURE 9

η , one must obviously compromise between fitting from too far (loss of accuracy in extrapolation) and fitting from too close (loss of accuracy owing to erratic behavior of functions). Further details are given under Program Degrees of Freedom.

The convergence procedure employed was initiated by establishing upper and lower limits for ϵ (denoted by ϵ_u and ϵ_l , respectively) and making an initial guess for $\epsilon = \frac{\epsilon_u + \epsilon_l}{2}$. A halving mode was followed until two values of N^* were recorded. Fig. 10 displays the principal operations involved. The tests indicated were applied after each integration step. It should be noted that the curve fitting procedure does not always yield values of \mathcal{J}^* and N^* , particularly during the early stages of convergence. In addition, for some combinations of η and step size, it is not possible to attain a value of \mathcal{J} between stations corresponding to $\mathcal{L}_0 = \eta a^*$ and $\mathcal{L}_0 = a^*$.

After obtaining two values of N^* , a linear prediction was made:

$$\epsilon'' = \epsilon_2 - N_2^* \left[\frac{\epsilon_1 - \epsilon_2}{N_1^* - N_2^*} \right]$$

If $\epsilon_l < \epsilon'' < \epsilon_u$, ϵ'' was used; otherwise it was discarded and the halving procedure was once again applied. This test suppresses the "overshoot" tendency of the slope technique in the nonlinear range. When all N^* had the same sign, the two smallest values were used. If both positive and negative values were available, the smallest value of each was used.

Typically, the reduction of N^* proceeded slowly until $N^* \sim O(10^{-3})$ owing to the fact that the halving technique was being used in this range. At this point the linear prediction came into play, resulting in order of magnitude reductions in a single iteration, e.g., decreases in N^* from $O(10^{-1})$ to $O(10^{-6})$ and from $O(10^{-6})$ to $O(10^{-10})$ for a given iteration have been noted. No particular advantage appears to be gained from

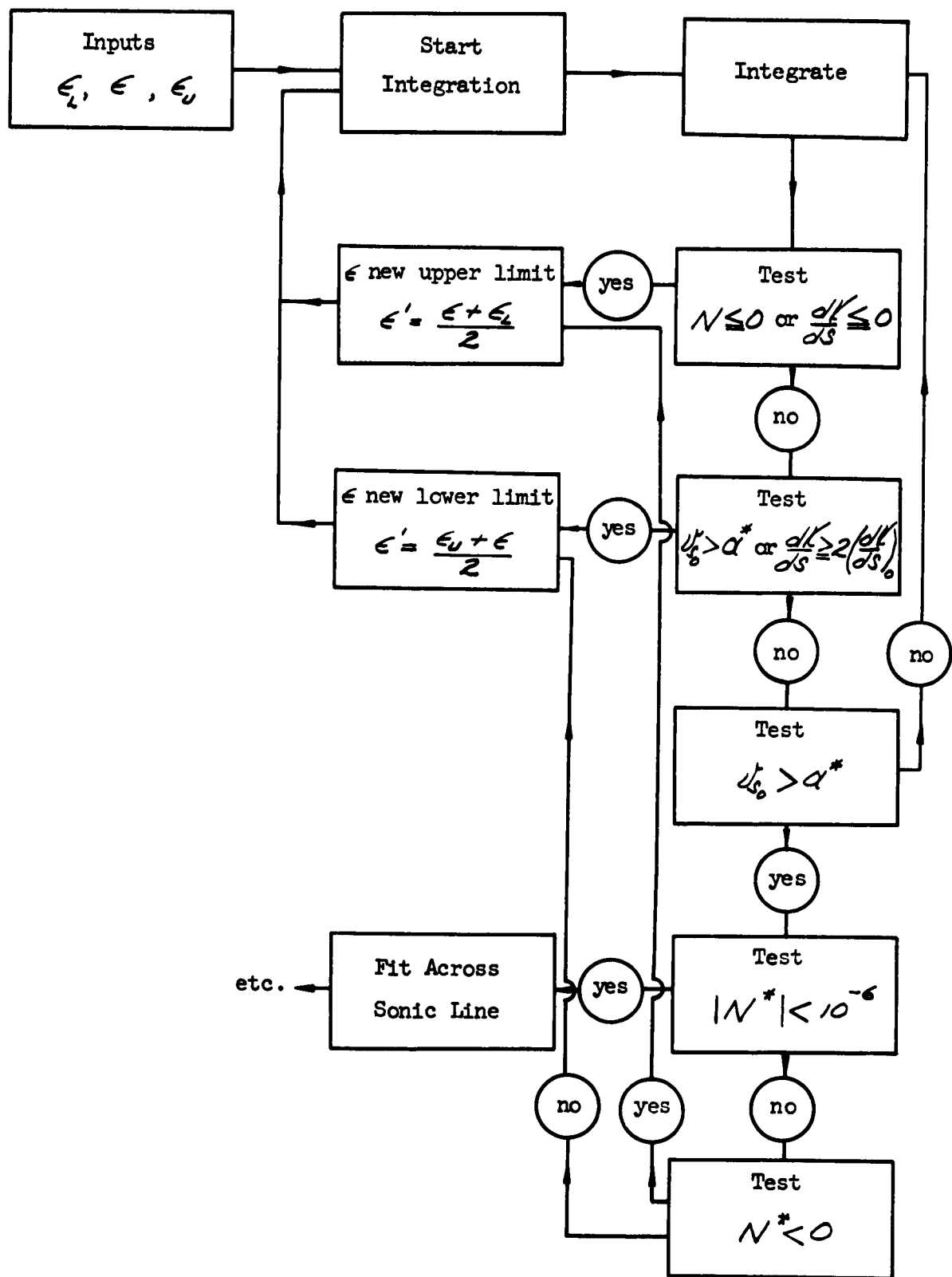


FIGURE 10 Halving Mode

reducing N^* below 10^{-6} . Figure 11 displays the variation of the \bar{F} versus S for $\epsilon = \bar{\epsilon}$.

No attempt was made to use polynomial extrapolation formulas of higher degree for estimating new values of ϵ . One disadvantage of increasing the degree is the associated requirement for more values of N^* , i.e., polynomial of degree m requires $m+1$ determining conditions.

For a given body shape and specific heat ratio, if a large number of runs corresponding to different values of M_∞ are to be made, one may expedite matters through use of polynomials of the form

$$\bar{\epsilon} = \sum_{n=0}^m \frac{C_n}{(M_\infty - 1)^n},$$

using the first few cases to determine the constants. Using a sixth degree polynomial, it was found that five reliable figures for $\bar{\epsilon}$ could be recovered, therefore reducing the number of iterations required.

4.2 Program Degrees of Freedom

Mechanization of the integral method introduces additional parameters which influence the numerical results. Their values are set primarily by an empirical approach using the computer as an experimental device. A brief discussion of their influence is given below. The data are taken from sphere calculations ($\gamma = 1.4$).

Integration step size: Table 1 indicates the ΔS effect on $\bar{\epsilon}$ and S^* for a fixed stopping condition $\psi_s \geq .95\alpha^*$. The fourth-order Runge-Kutta method of integration was employed in compiling these results. Use of other numerical integration schemes was not considered in the present investigation.

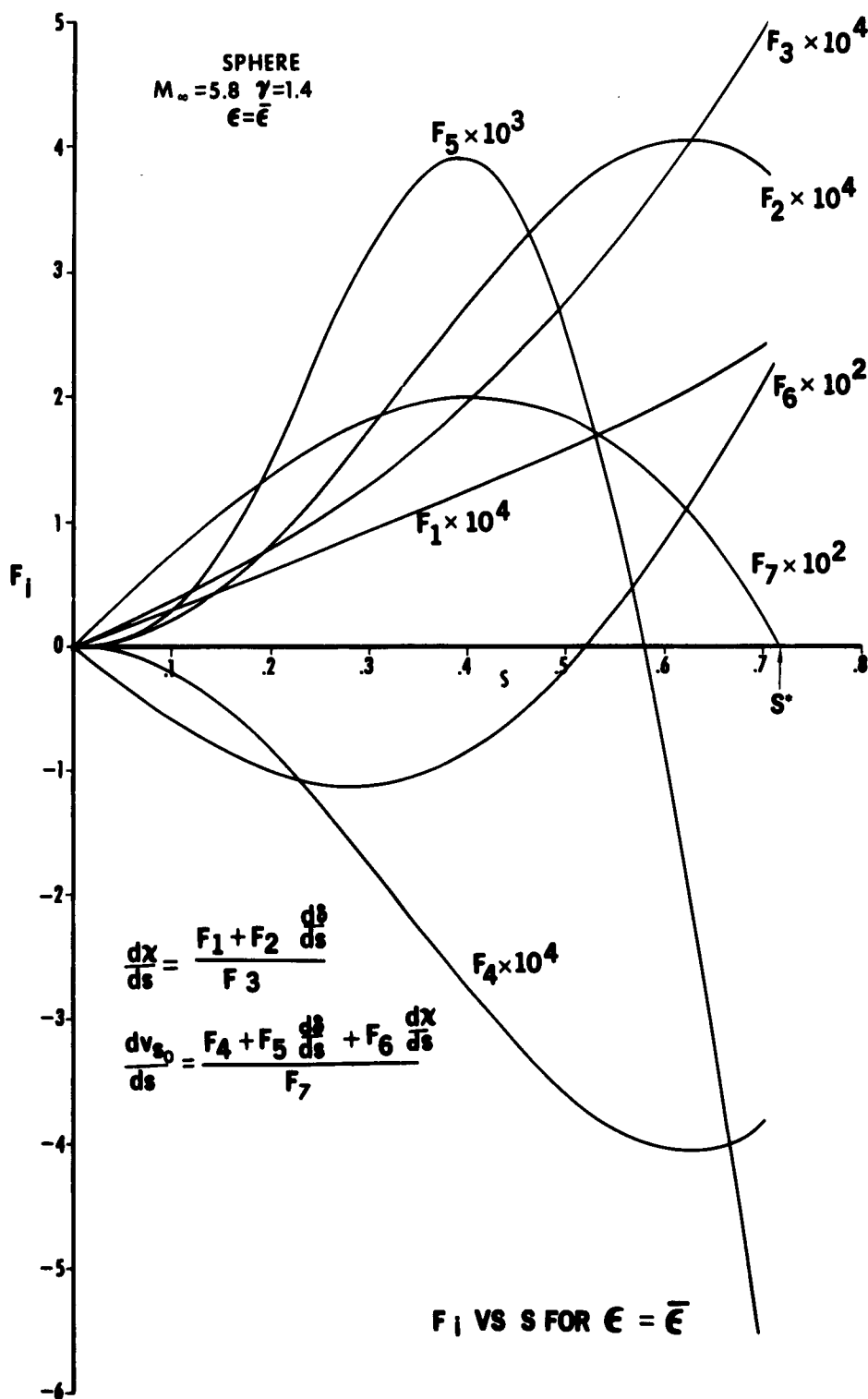


FIGURE 11

	ΔS	$M_\infty = 3$	$M_\infty = 6$	$M_\infty = 9$
$\bar{\epsilon}$.005	.21592940	.14823571	.13692880
	.01	.21592940	.14823570	.13692880
	.02	.21592943	.14823565	.13692875
S^*	.005	.76711752	.72000300	.71176106
	.01	.76712370	.71997798	.71176337
	.02	.76713051	.71991991	.71171965

TABLE 1

Near-sonic stopping condition: For those cases where $N^* > 0$, a criterion is required to stop the integration procedure short of the sonic point (defined by $D(S^*) = 0$). One may fix this point in terms of a physical location $S_s < S^*$ or may specify it in terms of a certain percentage, η , of the sonic velocity. Although the former method requires an approximate knowledge of S^* , a "linearizing" effect is introduced (see Figs. 12 and 13) with reference to the variation of N^* versus ϵ . Figs. 14 through 16 illustrate the influence of S_s on the standoff distance and sonic point location as well as the quantities ψ_s , $d\psi_s/ds$, f , df/ds , δ , $d\delta/ds$ evaluated at the downstream location $S = 1$. The latter plots are intended to indicate the increase in accuracy gained by fitting from a point closer to the sonic point. An asymptotic behavior is indicated but computational restrictions prevent determination of the final asymptotic value. The stopping condition $\psi_s \geq \eta \psi^*$ was found to be most convenient from a computing standpoint in spite of the disadvantage of fitting from different terminal values of S [depending upon the value of standoff distance chosen which in turn controls the functional behavior of $\psi_s(S)$]. More specifically, a randomness is introduced in the function $N^*(\epsilon)$ which can seriously impair slope prediction techniques. In addition, a ΔS influence is introduced unless a local adjustment of step size is made such that $\psi_s = \eta \psi^*$ precisely at the end of a given step. Table 2 indicates the effect of η on $\bar{\epsilon}$ and S^* .

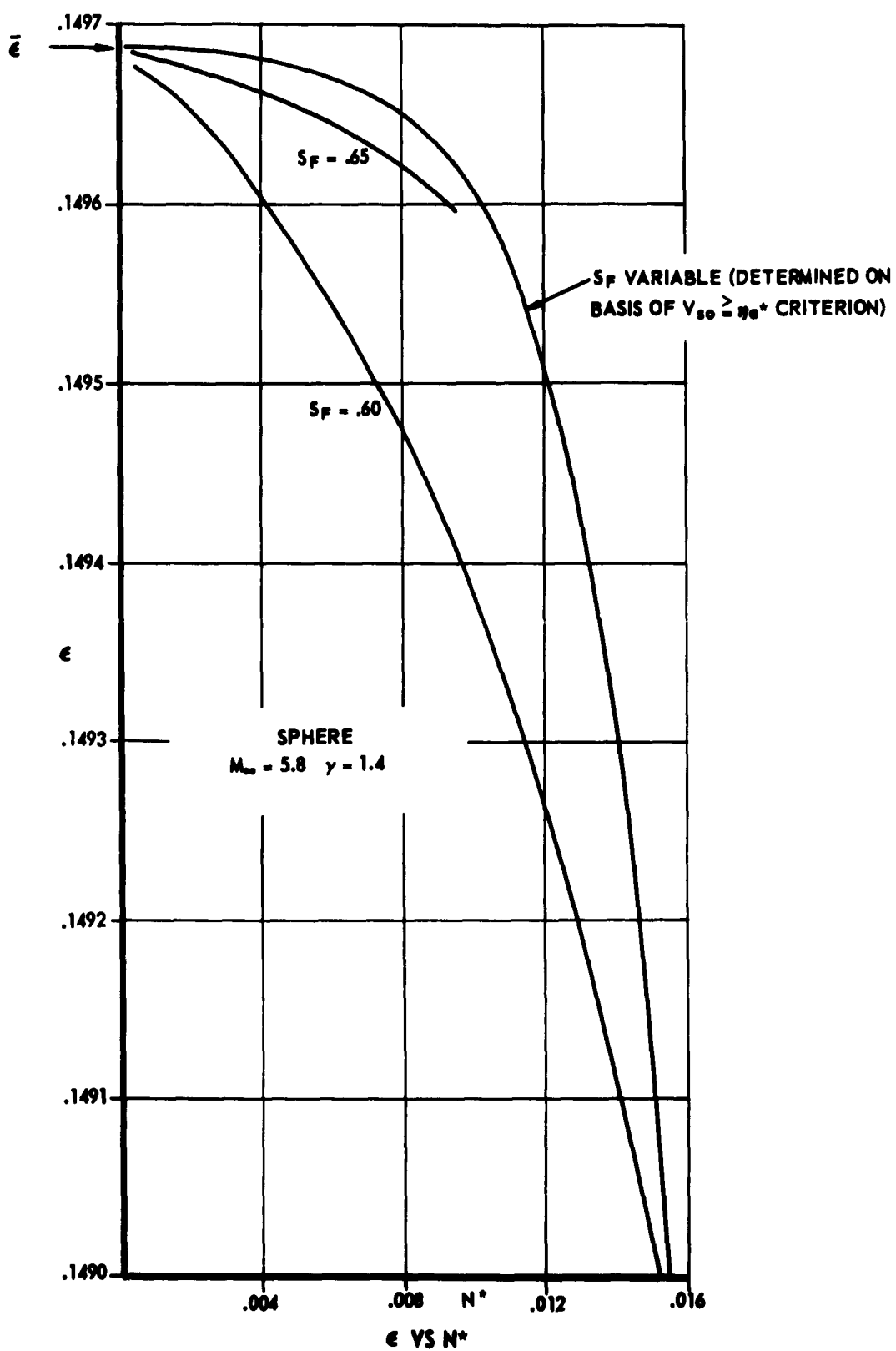


FIGURE 12

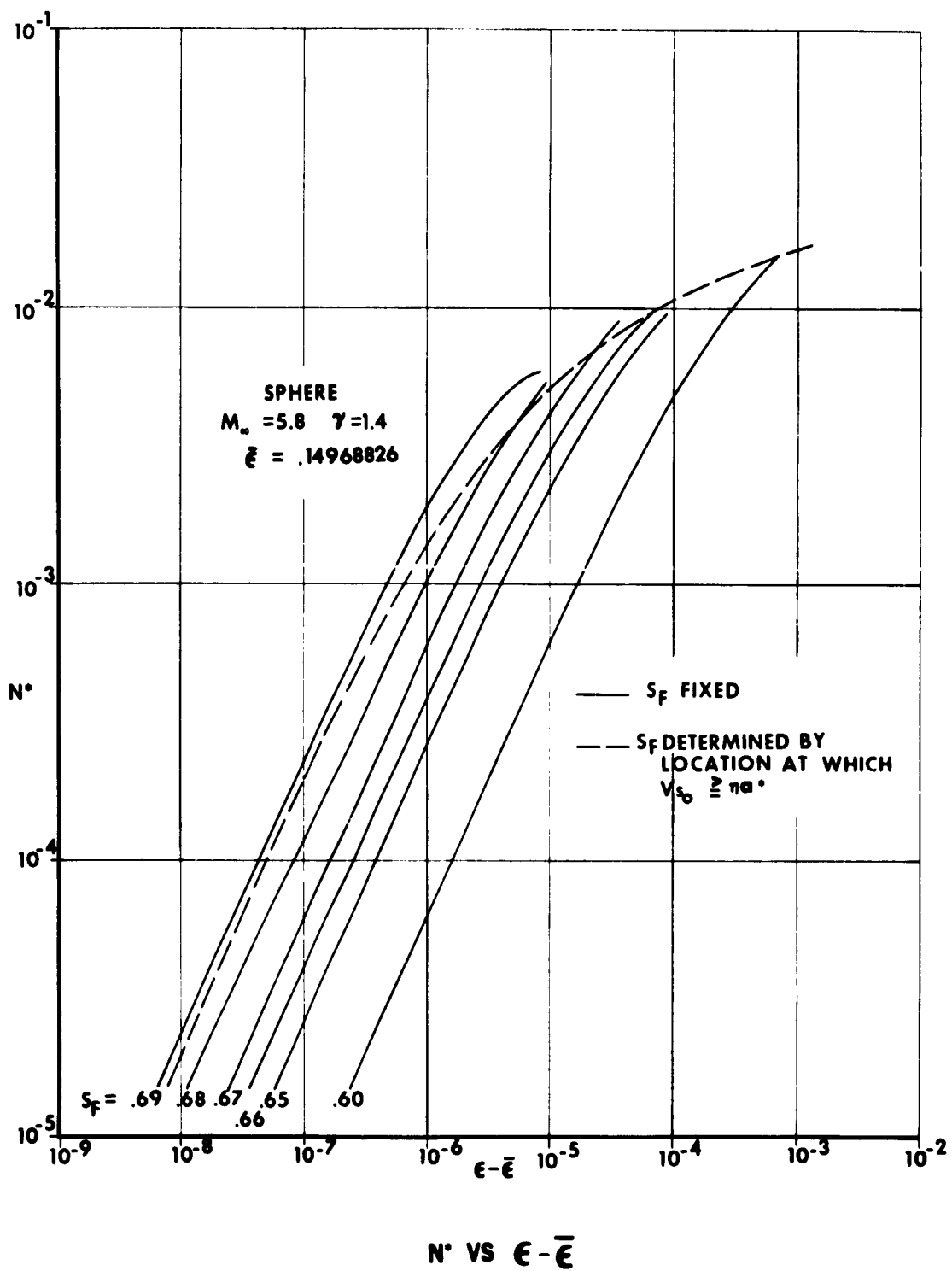
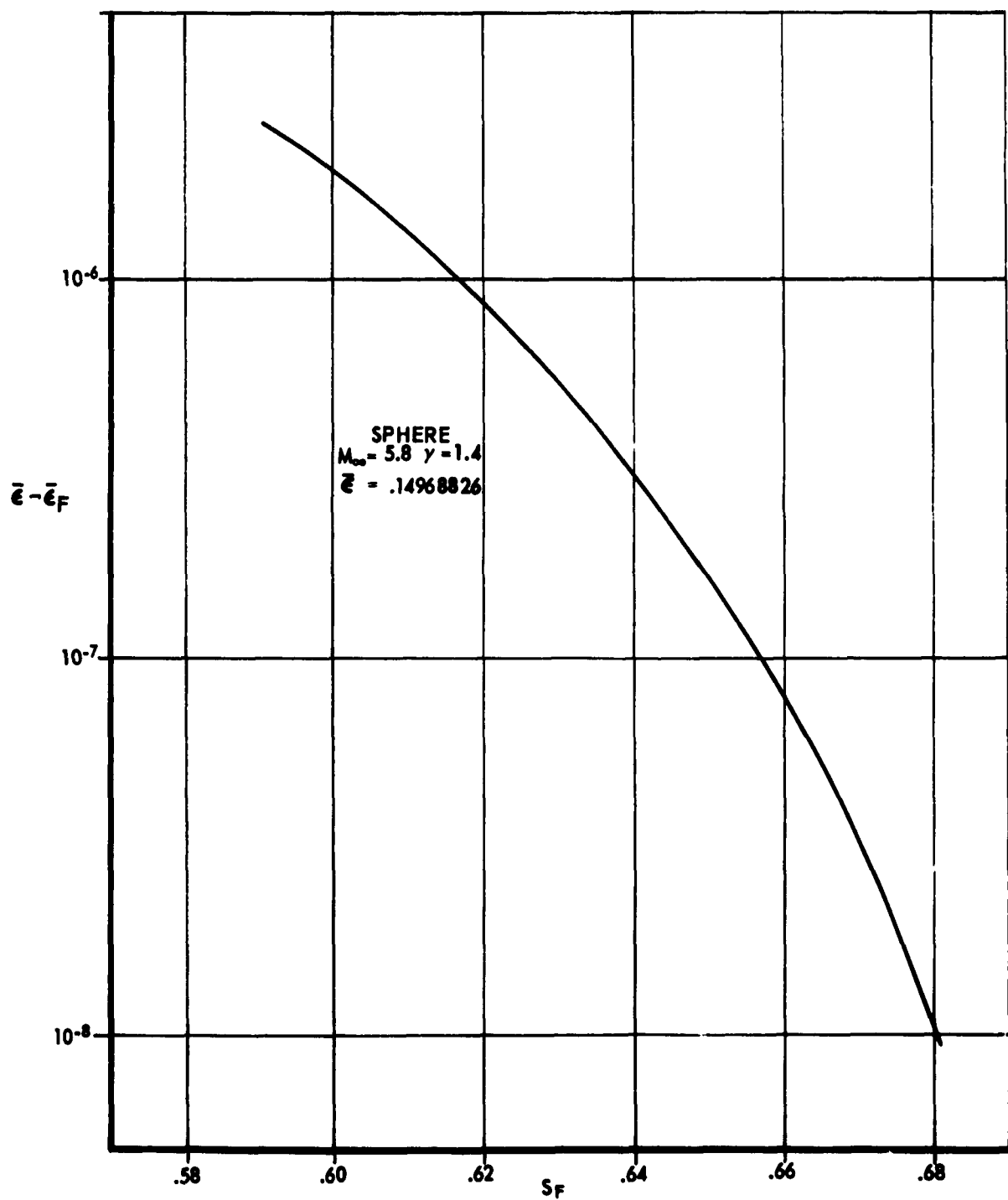


FIGURE 13



EFFECT OF FIT DISTANCE ON $\bar{\epsilon}$

FIGURE 14

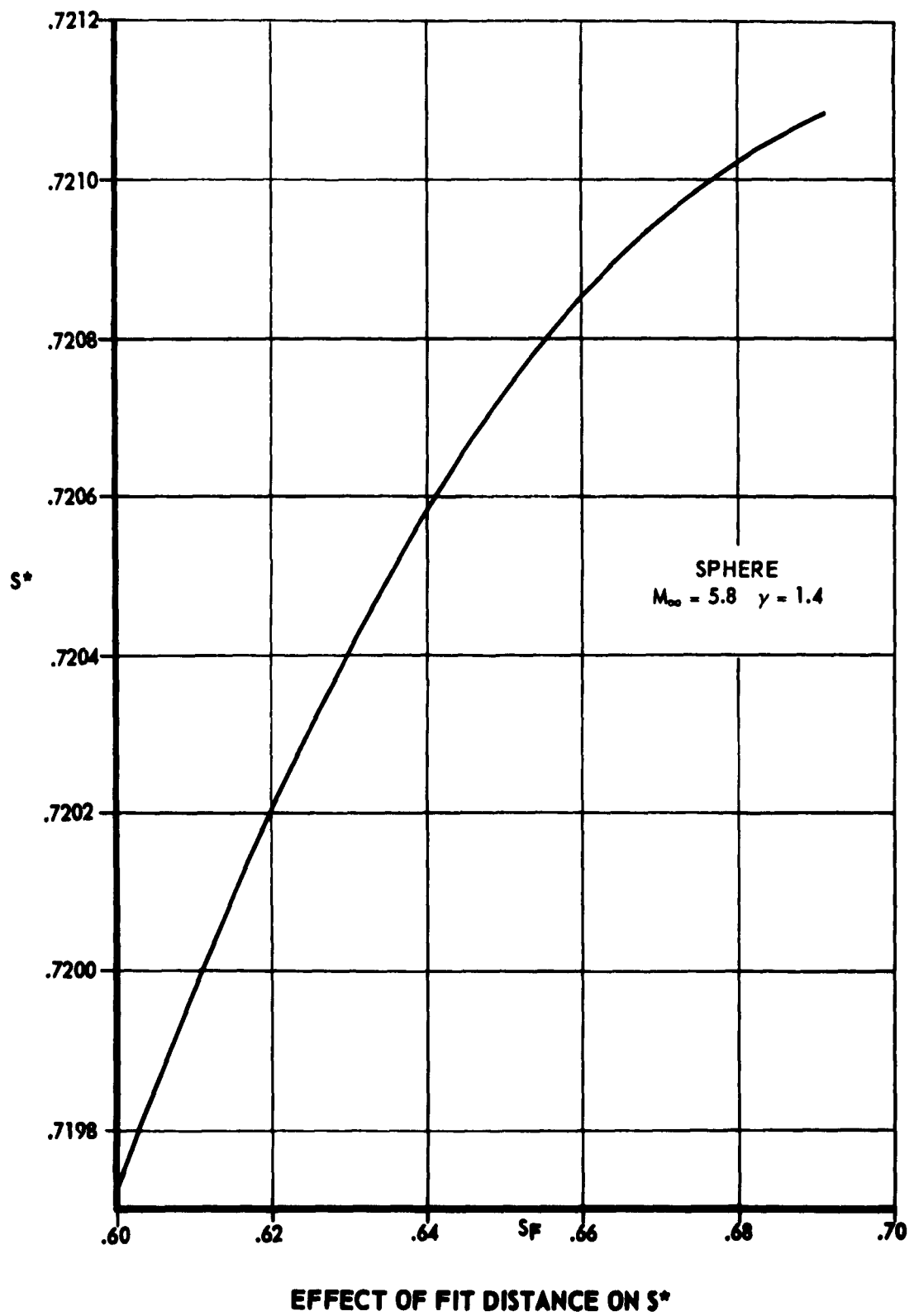
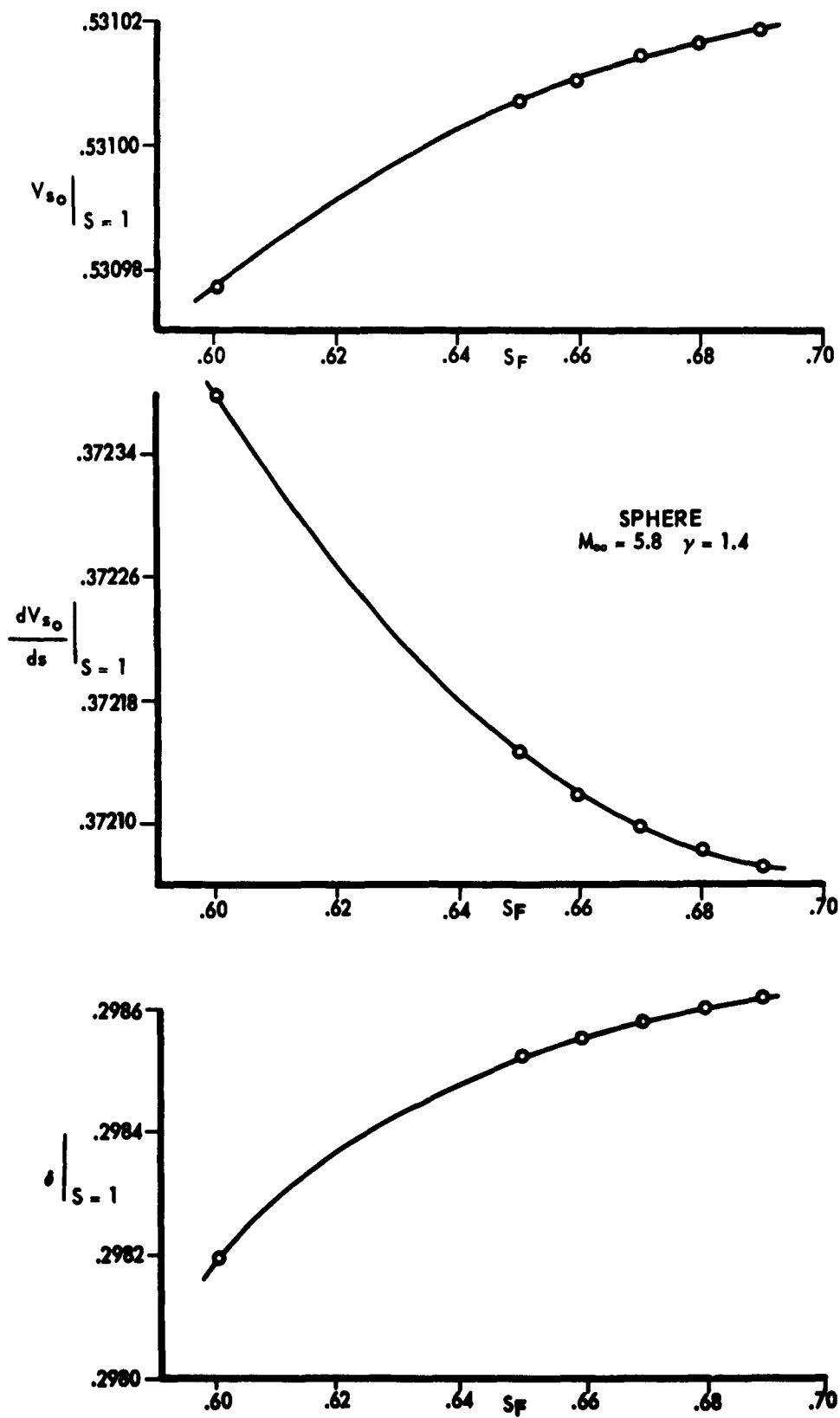
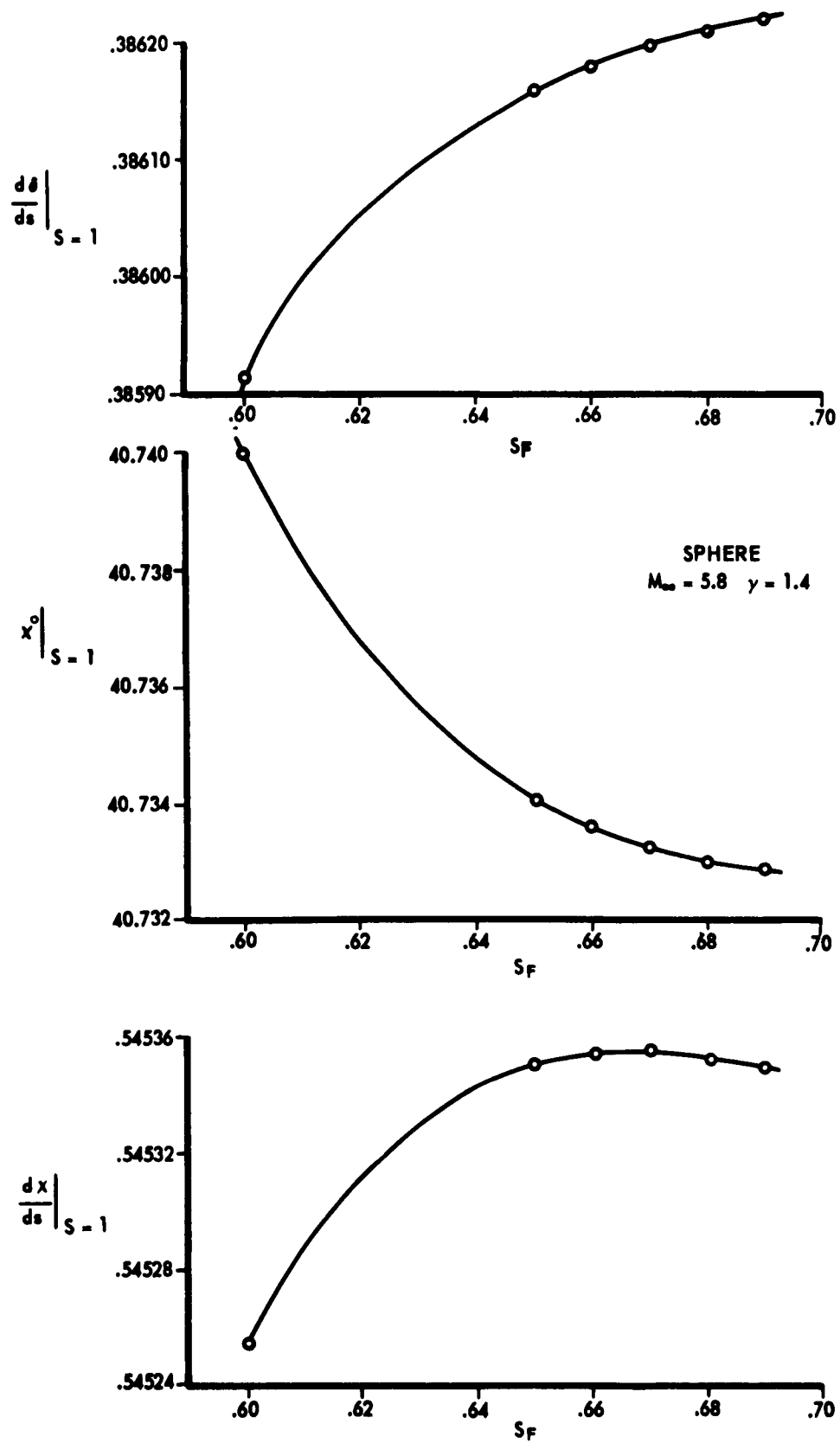


FIGURE 15



EFFECT OF FIT DISTANCE ON DOWNSTREAM VALUES

FIGURE 16



(CONT.) EFFECT OF FIT DISTANCE ON DOWNSTREAM VALUES

FIGURE 17

	η	$M_\infty = 3$	$M_\infty = 6$	$M_\infty = 9$
$\bar{\epsilon}$.975	.21592946	.14823571	.13692880
	.95	.21592940	.14823570	.13692880
	.90	.21592835	.14823543	.13692869
S^*	.975	.76717822	.72006109	.71182377
	.95	.76712370	.71997798	.71176377
	.90	.76682185	.71952513	.71135662

TABLE 2

Degree of curve fit: A quadratic expression was used for determining both S^* and N^* . Other investigators (e.g., Ref. 7) have employed cubic expressions. A parametric study of the influence of the degree of the curve was not made for smooth bodies; however, results pertaining to this topic are given later for the flat-faced cylinder case (see Applications).

5. CONVERGENCE SCHEME - BODIES WITH SONIC CORNER

As stated previously, the condition to be satisfied for bodies with a single convex corner at which sonic velocity is reached is simply given by

$$S^*(\bar{\epsilon}) = S_{\text{CORNER}}$$

The variation of S^* with $\bar{\epsilon}$ for a typical body displays none of the radically nonlinear behavior of the smooth body case. Through the use of a quadratic interpolation, the criterion $|(S^* - S_c)/S_c| \leq 10^{-5}$ was satisfied in a relatively small number of iterations. For the special case of a body with zero curvature up to the corner, i.e., flat-faced cylinder, cone with detached shock wave, no iteration is required in a strict sense since the relation is precisely linear. Further details are given under Applications.

6. INVERSE PROCEDURE

6.1 Iterative Method

Solution of the governing system of total differential equations yields $\delta(\zeta)$, $f(\zeta)$, $\psi_0(\zeta)$ and their derivatives. Since $r_0(\zeta)$, $\theta(\zeta)$, $R(\zeta)$ and $\phi(M_\infty)$ have been previously given, one may now determine ψ_0 , ψ_1 , ψ_2 , ζ , ρ , ρ_0 , ρ_1 , ρ_2 as functions of ζ . If one chooses to follow a formal inverse procedure in calculating shock layer properties, t_0 , t_1 , Z_0 , G_0 and G_1 must be evaluated. Hence $t(\zeta, \eta)$, $Z(\zeta, \eta)$ and $G(\zeta, \eta)$ are specified through use of Eq. (2-13). Finally ρ , ρ_0 , ψ_0 and ψ_1 are determined from the relations

$$\rho = \rho_0(1 - \psi_0^2 - \psi_1^2) \quad (6-1)$$

$$\rho = \left\{ \frac{G + t \left[j \cos \theta \left(1 + \frac{\rho}{R} \right) + \frac{r_1}{R} \right] \rho^{\frac{\gamma-1}{\gamma+1}}}{-\frac{r_1}{R} \rho t^2} \right\}^{\frac{\gamma+1}{\gamma-1}} \rho \quad (6-2)$$

$$\psi_0 = \left(\frac{\rho}{\rho_0} \right)^{\frac{\gamma-1}{\gamma+1}} t \quad (6-3)$$

$$\psi_1 = \frac{Z}{\rho \psi_0} \quad (6-4)$$

Since the pressure relationship obtained by substituting Eqs. (6-2), (6-3) and (6-4) into Eq. (6-1) is implicit in nature, an iterative solution is

required. Unfortunately, the solution has separate roots corresponding to $M \leq 1$, and switches roots along normals ($\psi = \text{constant}$ lines) crossing the sonic line. The calculated flow field in this region is always discontinuous since the expression does not allow a smooth transition from a subsonic body point to a supersonic shock point. In addition, $G \equiv 0$ for the case of a flat-faced cylinder and the system of equations becomes underspecified, i.e., only the Z and τ linear relations plus Bernoulli equation are available for determining ρ, p, ψ, ψ_n . This situation also arises when the system of equations is written directly in cylindrical polar coordinates (e.g., Ref. 8) since only two approximating functions are required.

6.2 "Linear" Method

Ref. 5 employs separate linear approximations for rg and $(1 + \frac{g}{R})\rho$ which leave the differential equations unchanged but lead to a simpler but overspecified algebraic procedure for determining the flow properties, i.e.,

$$\rho = \frac{1}{(1 + \frac{g}{R})} \left\{ \rho_0 + \frac{R}{g} \left[\left(1 + \frac{g}{R}\right) \rho_0 - \rho \right] \right\}$$

$$\psi = e^{\frac{g}{R}} \rho^{-\frac{1}{\sigma+1}} (g - k\rho)^{\frac{1}{\sigma+1}}$$

$$\rho = \frac{g - k\rho}{\psi^2}$$

$$\psi_n = \frac{Z}{\rho \psi}$$

$$\rho = \rho(1 - \psi^2 - \psi_n^2)$$

For a sphere calculation, this situation does not occur if polar coordinates $(\bar{r}, \bar{\theta})$ are used since the two terms collapse naturally to a simpler expression, i.e., using $n = \bar{r} - R$, $s = R\bar{\theta}$ and $r = \bar{r}\sin\bar{\theta}$, G reduces to $(\bar{r}\sin\bar{\theta})(\rho u_0^2 + 2kp)/R = \bar{r}\sin\bar{\theta}\bar{g}/R$. Ref. 9 represents \bar{g} linearly thus decoupling the \bar{r} term. This decoupling is not possible when representing $G(s, n)$ linearly; therefore, while the original governing equations in either s, n or $\bar{r}, \bar{\theta}$ coordinates are equivalent, the integral approximations employed are not equivalent.

The foregoing considerations indicate that use of a formal inverse procedure in the present one strip calculation leads to computational difficulties. Ref. 17 (two strip approximation) appears to circumvent this difficulty by abandoning the formal procedure and employing quadratic expressions involving values of the flow variables on the body, shock and the intermediate center strip.

6.3 Gradient Method

The derivatives of the flow variables in the s and n directions at the shock and body may be expressed entirely in terms of quantities yielded by the basic integration for \mathcal{S} , \mathcal{K} and \mathcal{U}_0 . This suggests a flow field determination based upon a knowledge of these gradients involving cubic approximations for three variables with the remaining variable being recovered from the Bernoulli equation and the entropy function.* An empirical procedure involving different combinations of cubic fits led to the use of the following system of equations (see Appendix I for the derivation of the gradient functions):

*It should be noted that an approximate higher order scheme involving gradients is discussed in Ref. 5 in which the one strip differential equations are modified with correction terms in an attempt to obtain improved body and shock data.

ρ , ρ and ψ_s are determined using expressions of the form

$$F = F_0 + \delta \left(\frac{\partial F}{\partial n} \right)_0 \frac{n}{\delta} + \left\{ 3(F_s - F_0) - \delta \left[2 \left(\frac{\partial F}{\partial n} \right)_0 + \left(\frac{\partial F}{\partial n} \right)_s \right] \right\} \left(\frac{n}{\delta} \right)^2 - \left\{ 2(F_s - F_0) - \delta \left[\left(\frac{\partial F}{\partial n} \right)_0 + \left(\frac{\partial F}{\partial n} \right)_s \right] \right\} \left(\frac{n}{\delta} \right)^3$$

ψ_n is subsequently determined from the Bernoulli equation with the cubic representation (denoted by a prime) being employed in order to fix the sign.

$$\psi_n = \frac{\psi_n'}{|\psi_n'|} (1 - \frac{\rho}{\rho_s} - \psi_s^2)^{\frac{1}{2}}$$

Also

$$\frac{s - s_{t_0}}{R} = \frac{1}{\gamma - 1} \frac{1}{2} \frac{\rho}{\rho_s} \gamma = \frac{1}{\gamma - 1} \frac{1}{2} \gamma$$

$$\theta_s = \theta + \tan^{-1} \frac{\psi_n}{\psi_s}$$

The aim of the foregoing procedure is to recover maximum information from those elements of the solution which most closely agree with experimental data. The usefulness of the gradient method will, of course, be diminished for those cases for which the shock and body values become less accurate.

7. CONSERVATION RELATIONS

A measure of the mathematical consistency of the gradient approach is afforded by determining the extent to which conservation laws are satisfied throughout the shock layer region. It has been noted (Ref. 10) that significant deviations in conservation of mass and momentum can occur in flow fields obtained using the integral method.

Considering the control volume shown in Fig. 17, the conservation equations are given by:

Mass:

$$\rho V_{\infty} (\pi r_f^2) \dot{r}_f = (2\pi) \int_0^{s(r)} \rho u_s r dr \quad (7-1)$$

Momentum:

$$\begin{aligned} (k\rho + \rho V_{\infty}^2) (\pi r_f^2) \dot{r}_f = (2\pi) \left[\int_0^{s(r)} (k\rho \cos \theta + \rho u_s u_x) r dr \right. \\ \left. + \int_0^s k\rho \sin \theta r ds \right] \end{aligned} \quad (7-2)$$

Energy:

$$\rho_{\infty} V_{\infty} (h_{\infty} + \frac{1}{2} V_{\infty}^2) (\pi r_s^2)_{\infty} = (2\pi) \int_0^{s(s)} \rho u_s (h + \frac{1}{2} V^2) r dr \quad (7-3)$$

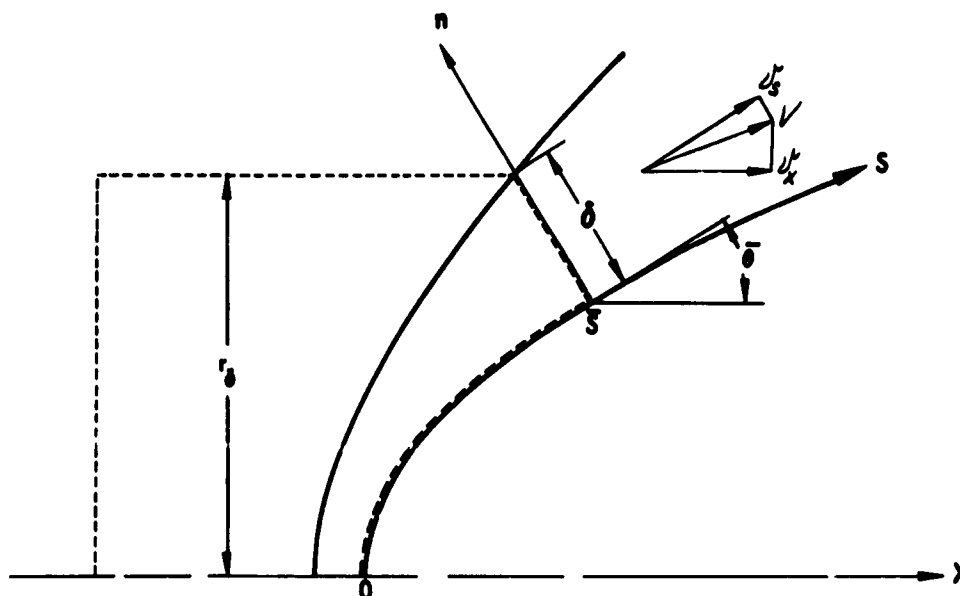


FIGURE 17

For an adiabatic flow process involving a thermally and calorically perfect gas, $h = \frac{1}{2} P/\rho$ (h nondimensionalized using V_{max}^2); therefore, using Eq. (2-7), the integral form of the energy relation reduces to the form of the mass conservation equation.

Defining

$$\tilde{m}(s) = \frac{2 \int_0^{s(s)} \rho u_s r dr}{\rho_{\infty} V_{\infty} s^2} - 1 \quad (7-4)$$

$$\tilde{M}(\mathcal{S}) = \frac{2^j \left[\int_0^{\mathcal{S}(\mathcal{S})} (\mathcal{L}p \cos \theta + \rho \mathcal{U}_x) r dr + \int_0^{\mathcal{S}} \mathcal{L}p \sin \theta r d\mathcal{S} \right]}{(\mathcal{L}p + \rho V_\infty^2) \mathcal{S}^{j+1}} - 1, \quad (7-5)$$

values of \tilde{m} and \tilde{M} have been computed for a number of cases. The results are presented in Figs. 18 through 20. The deviations noted are primarily a consequence of the inverse procedure employed to recover the flow variables.

7.1 Sphere Results

Fig. 18 presents a comparison of the deviations from mass conservation resulting from application of the "linear," iterative and gradient inverse methods for $\mathcal{M}_\infty = 3, 6, 9$. A single ($\mathcal{M}_\infty = 6$) curve is presented for the iterative method. The break in this curve corresponds to the "double-valued" region mentioned previously. From a practical standpoint, the deviations occurring in the range corresponding to low supersonic Mach numbers in the field ($.8 < \mathcal{S} < .9$) are particularly significant in that starting solutions for characteristics are derived from the flow field results in this region. Suppression of errors which could subsequently propagate into the downstream field is therefore necessary in this range. In this respect, the gradient method provides a substantial improvement over the other techniques. Conservation of momentum deviations are also significantly reduced through use of the gradient method (Fig. 19).

7.2 Flat-Faced Cylinder Results

As indicated previously, the need for two of the approximating functions vanishes in the case of the flat-faced cylinder. A decision was made to retain these relations in determining the flow field since the approximations consistent with this "linear" inverse method appear to have more validity than the gradient method on the basis of results shown in Fig. 20. Since the accuracy of the gradient method is directly related to the

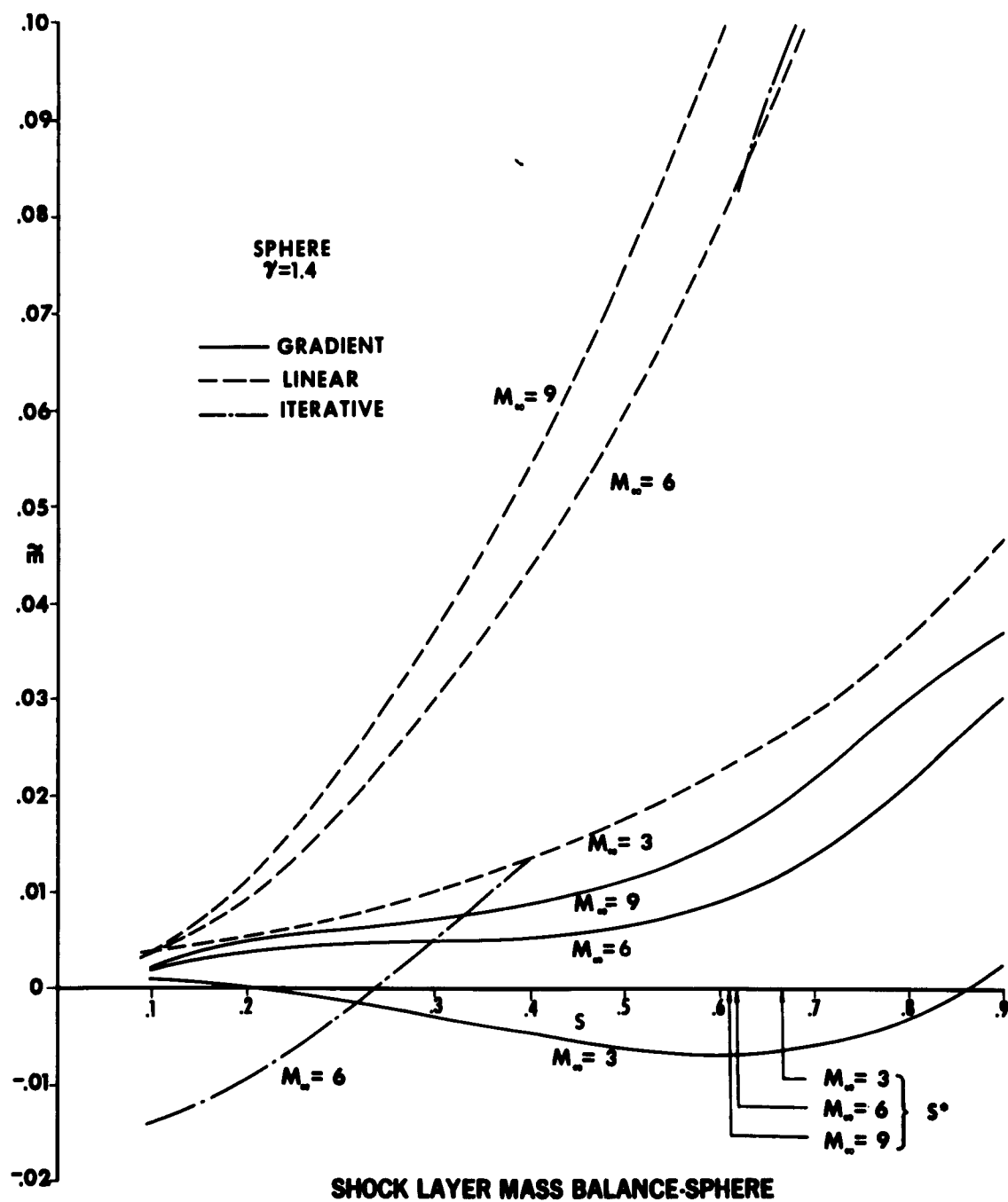


FIGURE 18

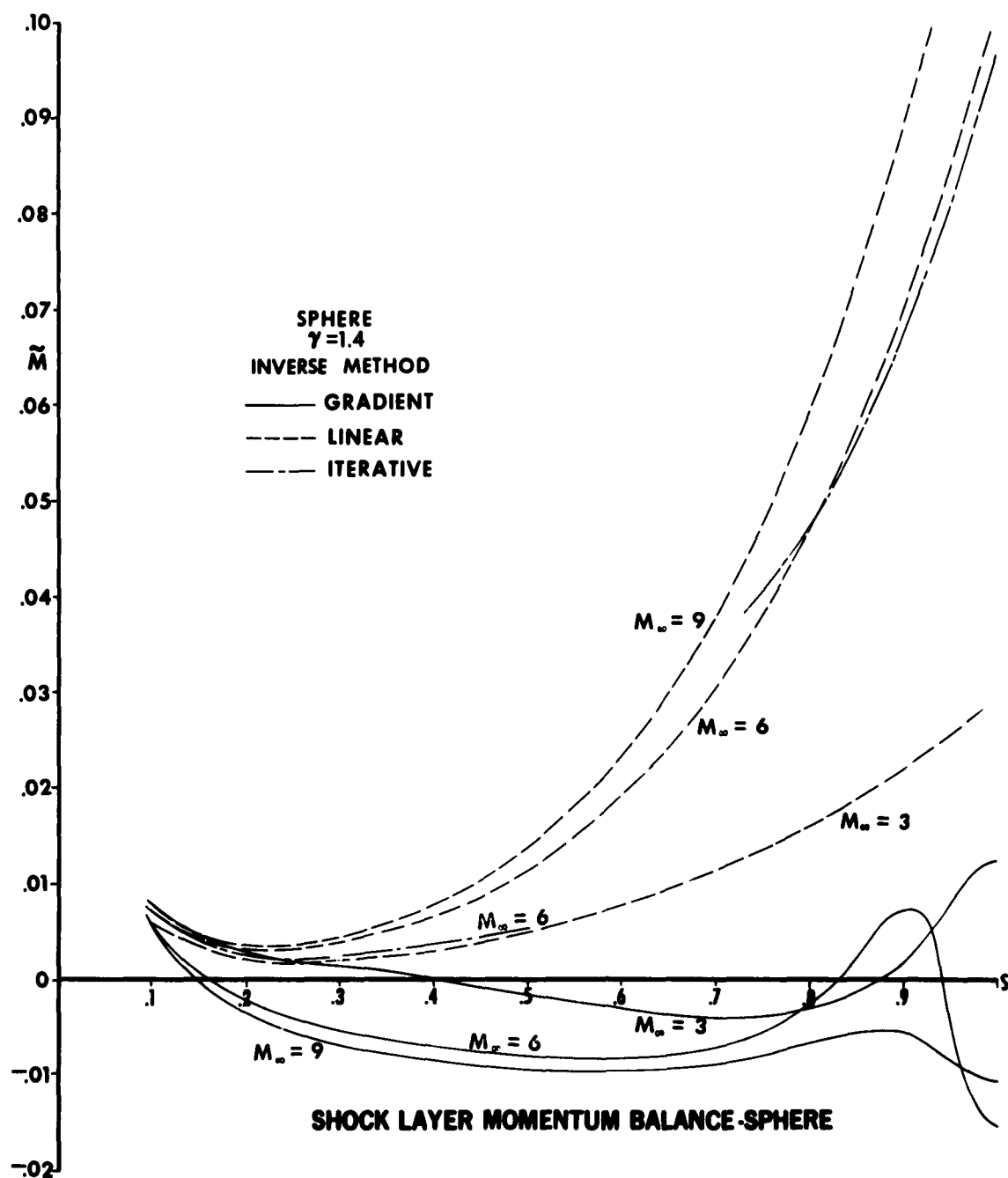
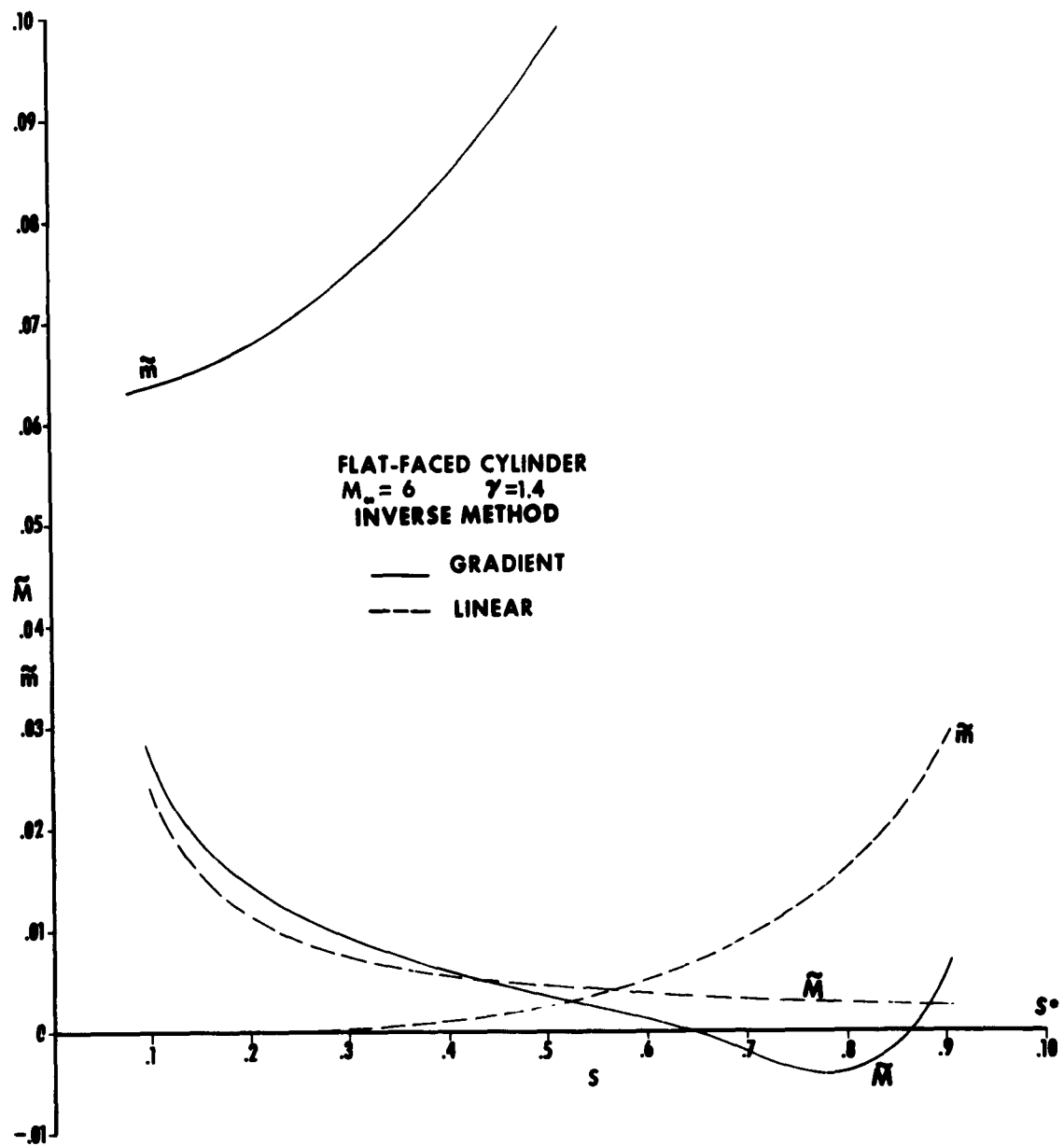


FIGURE 19



SHOCK LAYER MASS AND MOMENTUM BALANCE
 FLAT-FACED CYLINDER

validity of shock and body data, particularly "second-order" quantities such as R_s and du_s/ds , the deviations in $\tilde{m}(\beta)$ may be interpreted as an indication of shortcomings in the basic solution for this body shape and at the given free stream conditions.

8. APPLICATIONS

The success of the one strip integral method in predicting shock shapes and surface pressure distributions has been established by previous investigators, excepting those cases where M_∞ is too close to unity or where rapid changes in body curvature are involved. Unfortunately, little information is available for determining the accuracy of the distribution of flow properties across the shock layer [sonic line data (Ref. 11) and interferometric ballistic range data (Ref. 12)].

In view of the preceding considerations, the results presented do not include experimental data but are intended to typify the information yielded by the integral method.

8.1 Sphere

The variation of shock detachment distance with free stream Mach number for $\gamma = 1.4$ is given in Fig. 21. A sixth degree polynomial of the form

$$\bar{\epsilon} = C_0 + \frac{C_1}{M_\infty - 1} + \frac{C_2}{(M_\infty - 1)^2} + \dots + \frac{C_6}{(M_\infty - 1)^6}, \quad C_0 = (\bar{\epsilon})_{M_\infty \rightarrow \infty}$$

was fitted to the numerical data in order to provide accurate detachment distances for intermediate Mach numbers (which are usable in the present formulation to approximately five decimal places as initial $\bar{\epsilon}$ values). A few cases were run for $\gamma \neq 1.4$ (e.g., for $\gamma = 1.2$ and $M_\infty = 20$, $\bar{\epsilon} = .073666$) which displayed trends in accord with the results of other theoretical methods. A plot of sonic point location versus M_∞ is also included (Fig. 22). For $M_\infty > 4$, a crossplot indicated that the relationship between $\bar{\epsilon}$ and \mathcal{J}^* becomes nearly linear. Fig. 23 presents the

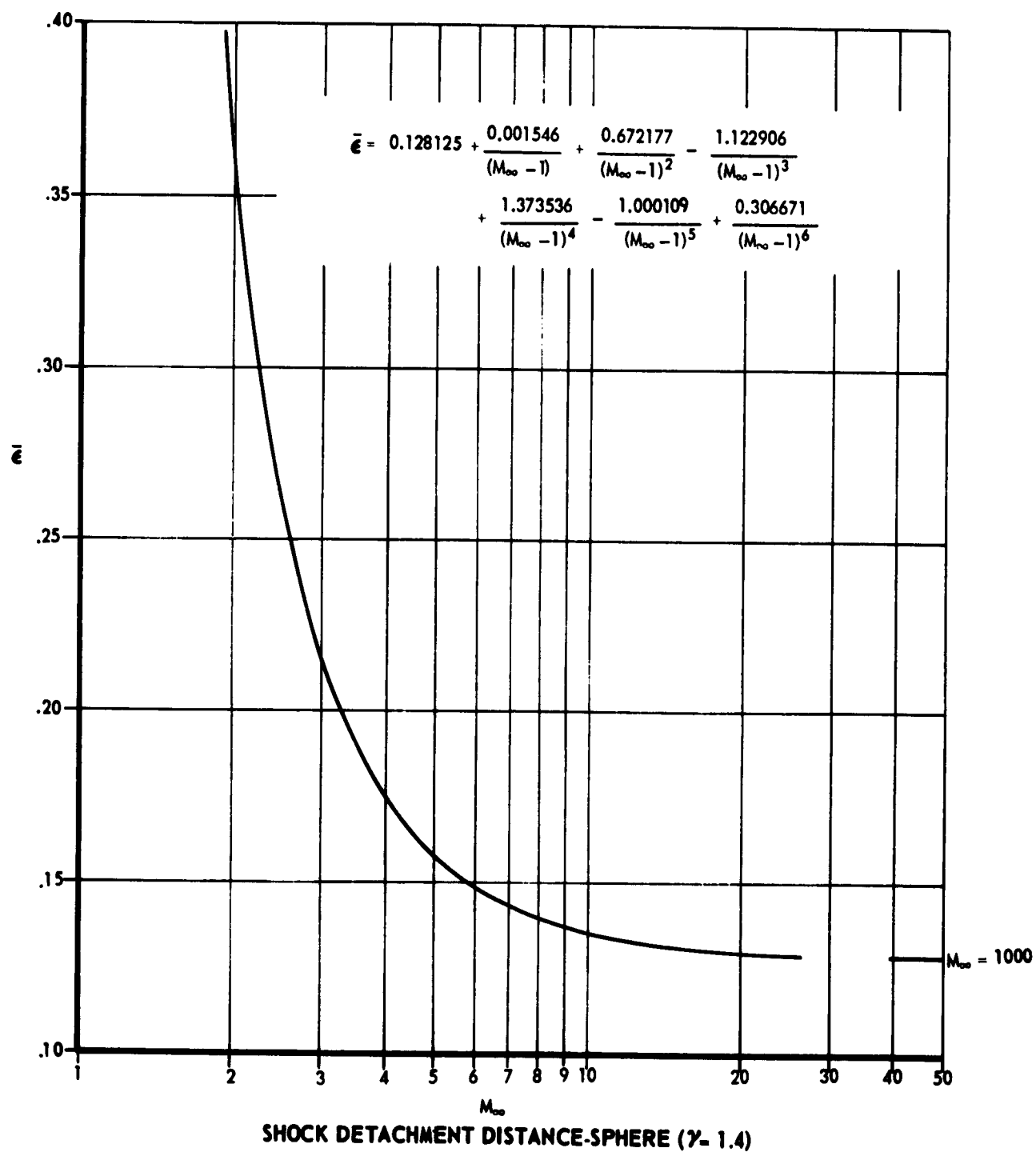
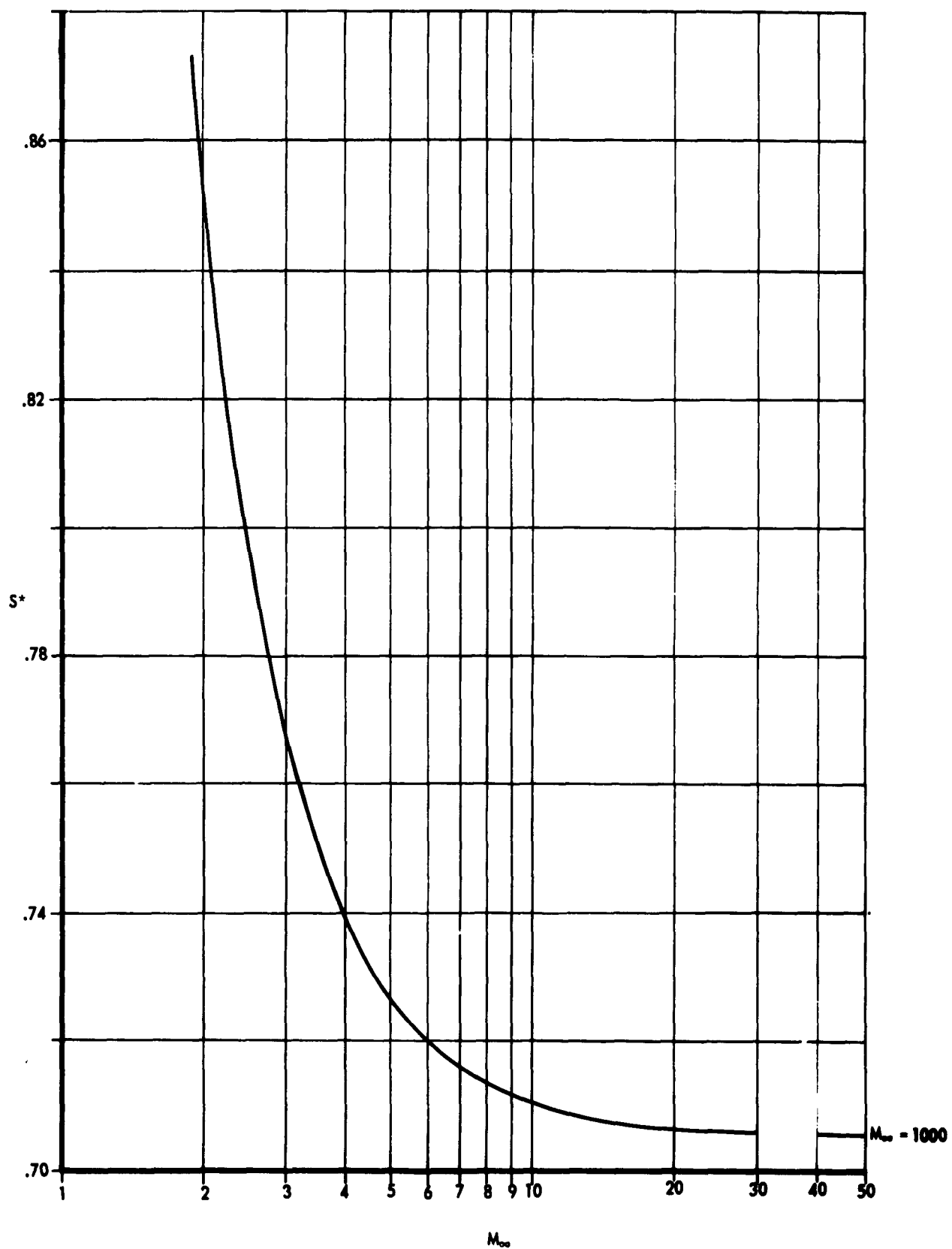


FIGURE 21



SONIC POINT LOCATION-SPHERE ($\gamma=1.4$)

FIGURE 22

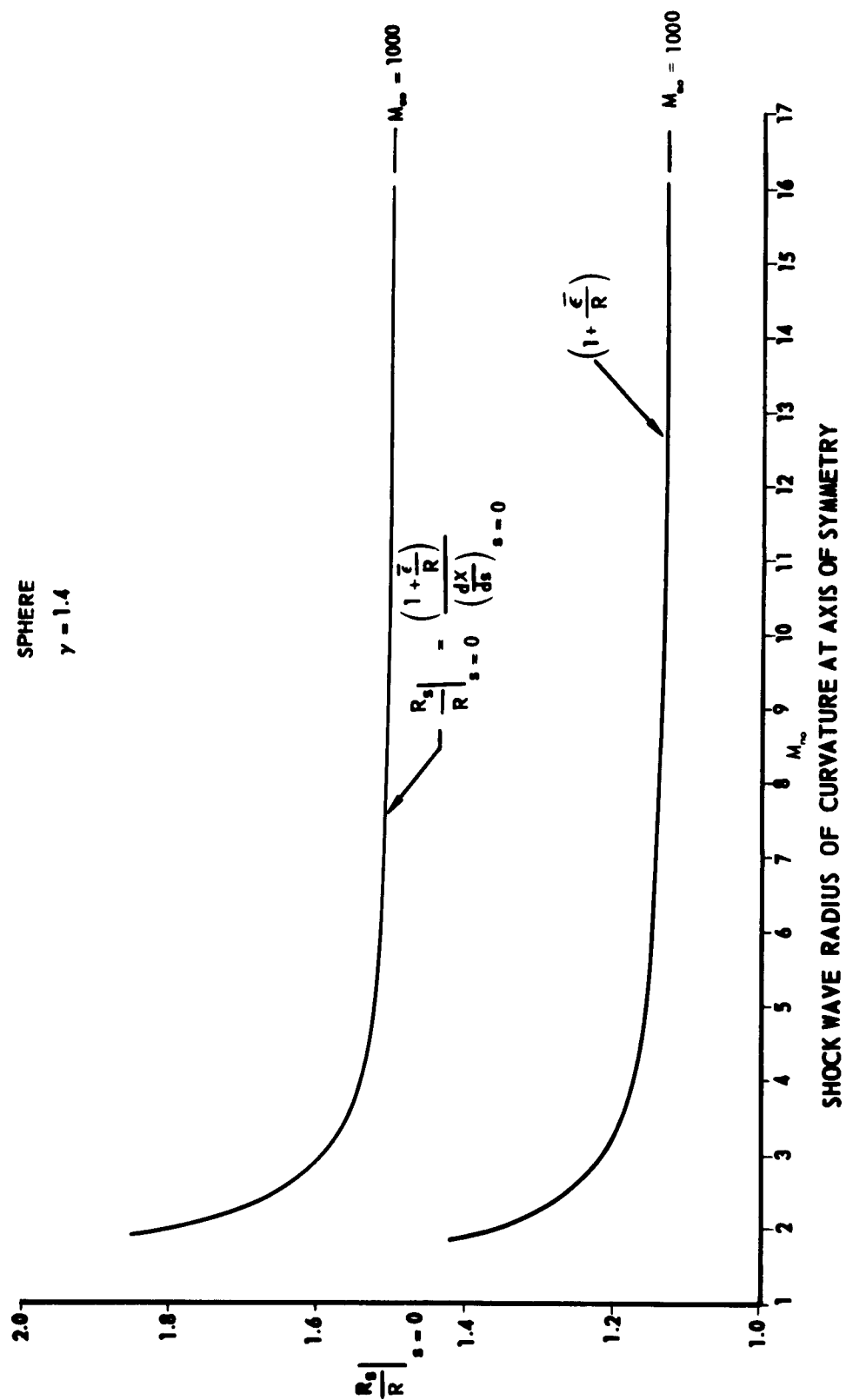


FIGURE 23

variation of shock radius of curvature at the axis with M_∞ . The limiting value of R as $M_\infty \rightarrow \infty$ is significantly higher than the corresponding result obtained by assuming a concentric shock wave, i.e., $R_c = R + \bar{e}$.

The distribution of flow properties across the shock layer was determined by means of the gradient method. In particular, the variations of $\rho(s, r)$, $\rho(s, r)$ and $M(s, r)$ are shown in Figs. 24, 25 and 26, respectively, for $M_\infty = 6$ and $\gamma = 1.4$. The density plot displays the small ρ variation in the stagnation region which is the physical basis for a number of approximate constant density solutions.

Fig. 27 gives a comparison of shock shapes derived through use of the method of characteristics (with an integral method starting line) and the integral method alone. The characteristic separating the sphere ($0 \leq \theta \leq \frac{\pi}{2}$) region of influence and the region additionally influenced by the afterbody is indicated in order to illustrate the "illegal" disturbance imposed in the integral method by change in afterbody geometry.

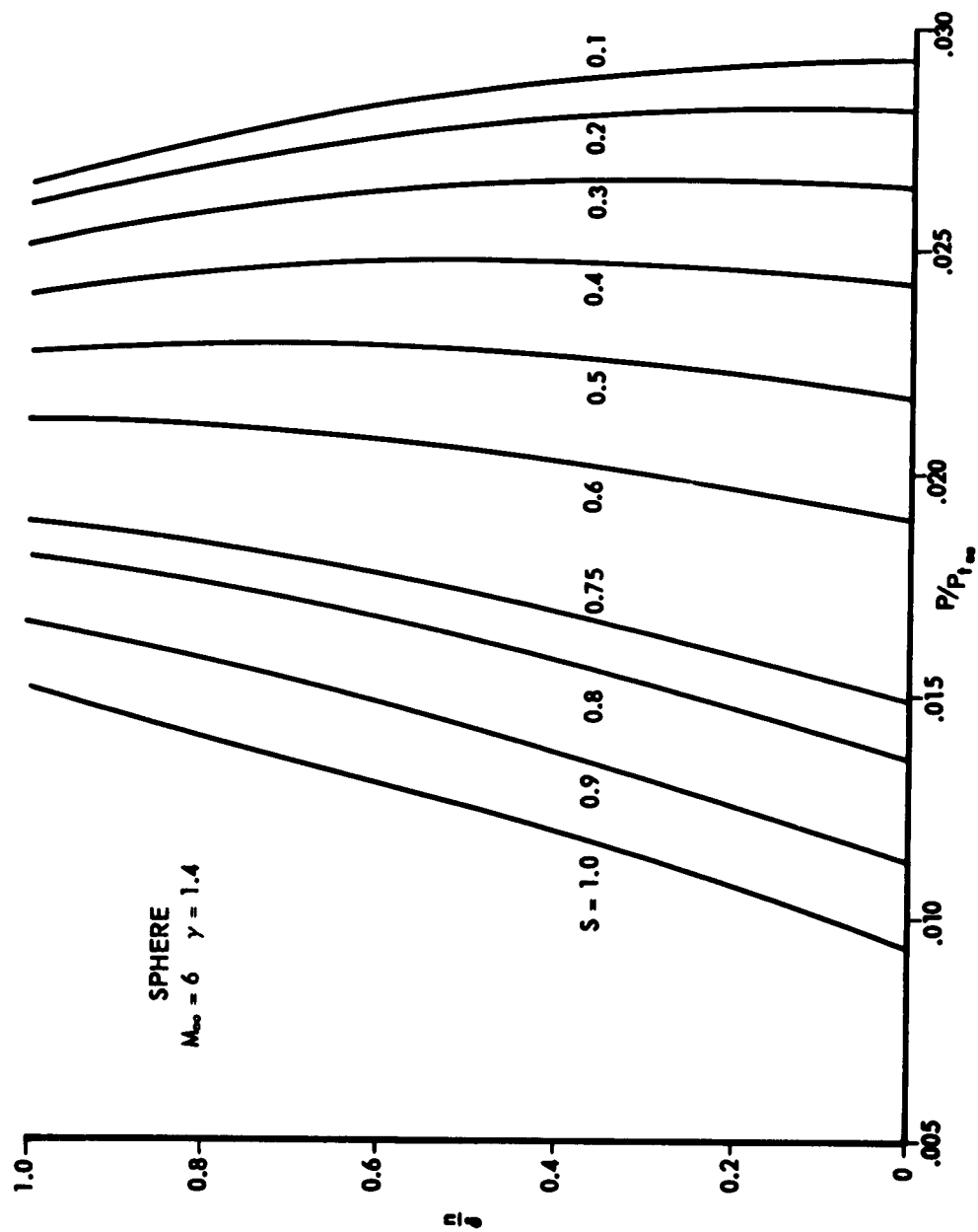
Typically, as the free stream Mach number is increased, the integral method shock wave tends to be farther below the true shock location (as defined by characteristics and experiment) for $K/R > 2$. It is interesting to note that for a complete sphere the integration into the supersonic regime continues smoothly until \mathcal{S} approaches $\pi - \mu_\infty$,

$\mu_\infty = \sin^{-1} \frac{1}{M_\infty}$. Below this point the normal to the sphere cannot intersect the shock wave. For example, for $M_\infty = 1000$, the integration proceeded up to $\mathcal{S} = 3.13$, i.e., 179.3° around the sphere!

8.2 Flat-Faced Cylinder

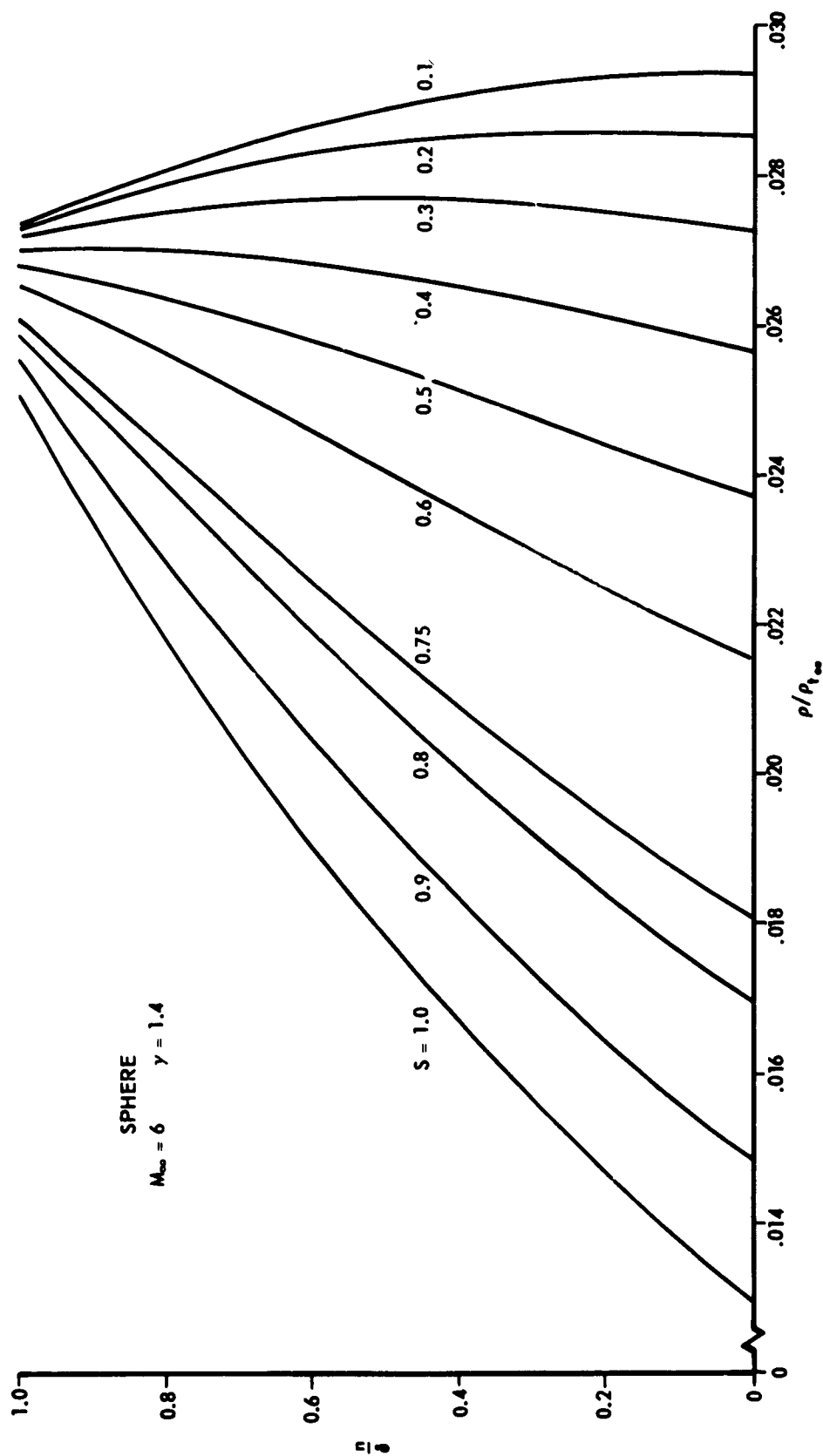
The parameters which control a given integration are

$$\bar{e}, \quad \delta(s), \quad \theta(s), \quad \frac{d\theta}{ds}$$



SHOCK LAYER PRESSURE DISTRIBUTION-GRAIENT METHOD

FIGURE 24



SHOCK LAYER DENSITY DISTRIBUTION-GRADIENT METHOD

FIGURE 25

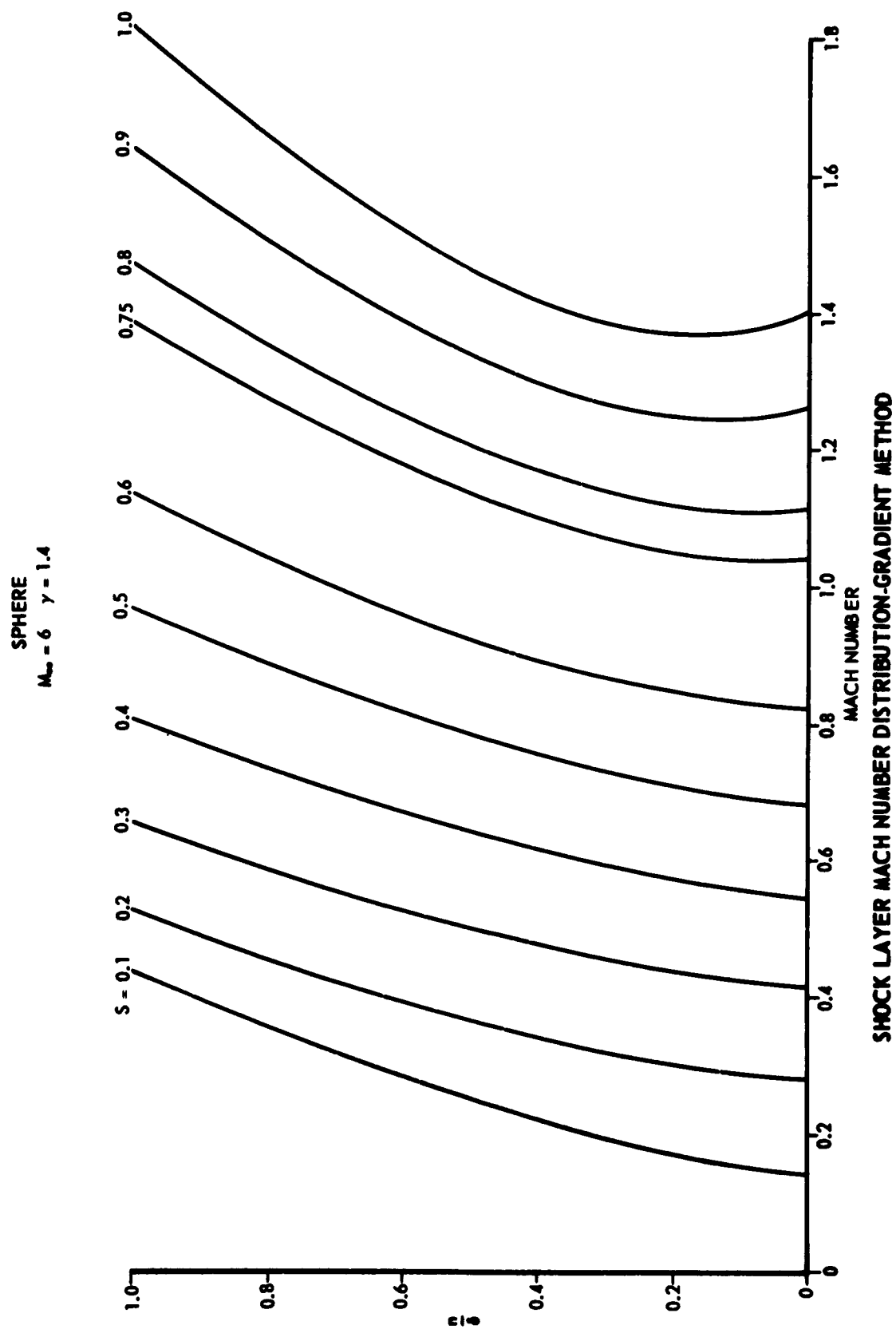


FIGURE 26

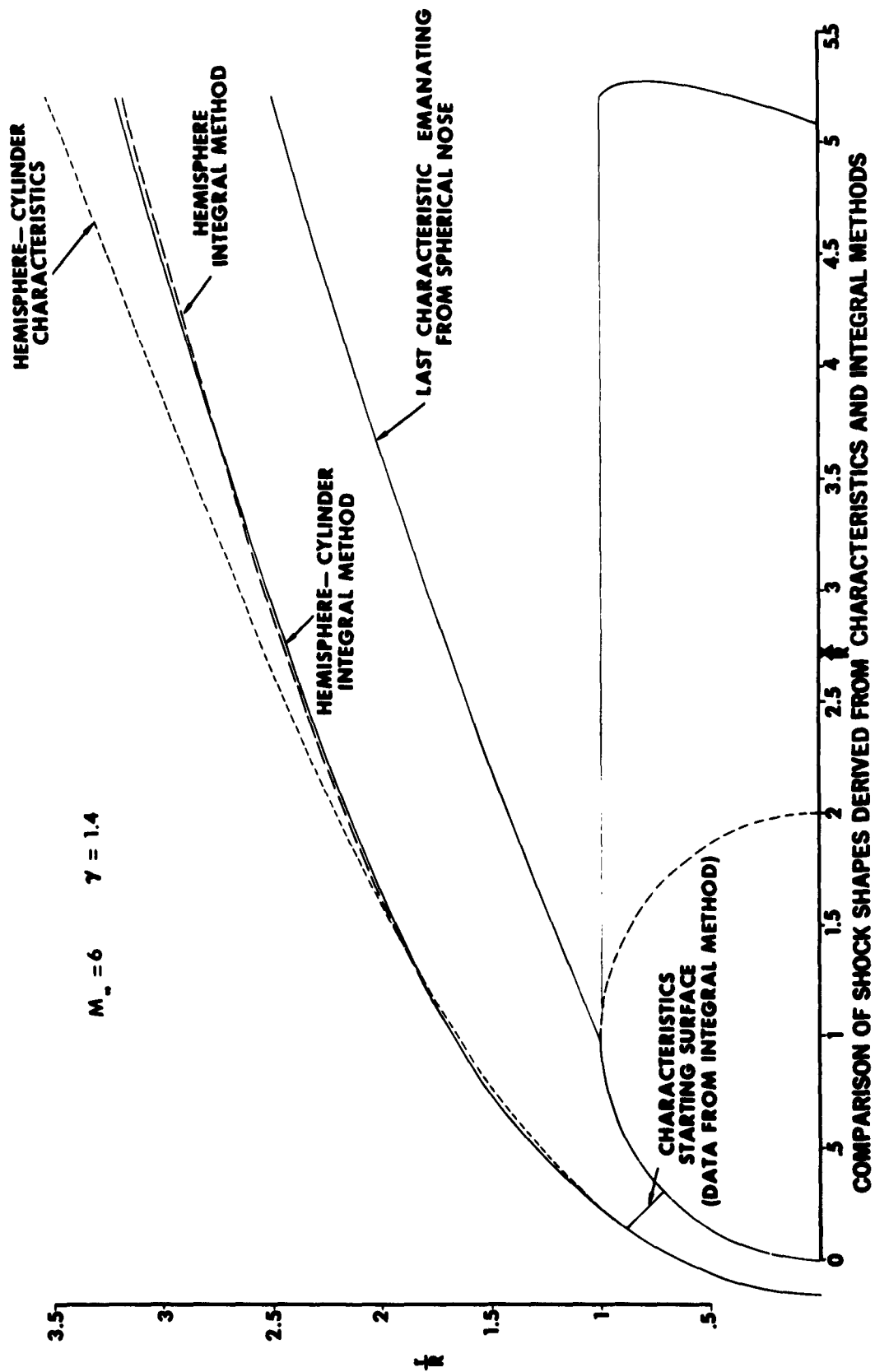


FIGURE 27

For conical or wedge nose caps terminating in a sonic corner ($\theta_{\text{DETACHMENT}} < \theta \leq \frac{\pi}{2}$), the latter two parameters become fixed and become directly proportional to the independent variable ζ .^{*} As a result, no coupling exists between $\bar{\epsilon}$ and the geometrical parameters as the integration progresses. The location of the body sonic point which serves as the only characteristic dimension remaining in the problem therefore becomes purely a function of $\bar{\epsilon}$. Hence, a scaling is implied which allows one to fix the sonic corner radius, ζ^* , at a prechosen value employing a maximum of two integrations. The first integration establishes the ratio

$$K = \frac{\bar{\epsilon}}{\zeta^*}$$

and the second integration serves to adjust ζ^* to a convenient reference value using $\bar{\epsilon} = K\zeta^*$ (in the present case, ζ^* was chosen as unity). The latter operation was found to be more convenient than one involving a storage of all quantities to be scaled.

Since the accuracy of the integral method is directly related to the approximations governing functional behavior in the η -direction, the validity of employing results derived from local transonic solutions (Ref. 16) within the framework of the computing procedures was checked in the following manner. The scaling property of the flat-faced cylinder case provided a means for determining the consistency of using the functional form suggested by second-order transonic theory for the surface velocity extrapolation formula at the corner, i.e.,

$$q^* - q_0^* = c(\zeta^* - \zeta)^2, \quad c = \text{const.}$$

^{*}A reformulation in terms of the coordinate system employed is necessary to handle cases for $\theta < \frac{\pi}{2}$. In this instance, ζ would be replaced by a corresponding variable.

$$\left(\frac{dU_0}{ds}\right)_{s=s^*-\epsilon} = \frac{-\epsilon n}{(s^*-s)^{1-n}}$$

For $0 < n < 1$, this expression allows the upstream surface velocity gradient to approach an infinite value at the corner (as dictated by inviscid flow theory).

The success of the scaling procedure was influenced by the choice of the exponent n . For example, a value of $n = \frac{1}{2}$ yielded a sonic corner radius of 1.0000001 while a value of $n = \frac{2}{5}$ (given by second order theory) gave a "less precise" scaling, $s^* = 1.0000044$. A weak dependence upon n therefore exists. In addition, numerical determination of n in an inverse fashion employing the last valid points computed near the corner yielded a value of 0.4996. Finally, employing a cubic fit which is in direct contradiction to the requirement that $(dU_0/ds)_{s=s^*-\epsilon} \rightarrow \infty$ as $\epsilon \rightarrow 0$ gives the poorest scaling, $s^* = 1.0004$.

From a practical standpoint, the preceding arguments become somewhat academic if the integration is not continued past the sonic corner since upstream flow field results are not significantly affected by the fitting procedures.

Owing to the steepening of the velocity gradient near the corner, a step size reduction was introduced as the corner was approached. This effect became particularly critical as the Mach number was decreased. The reduction criterion was based on a test of dU_0/ds rather than U_0 owing to the rapid divergence of the velocity gradient expression within the span of a few integration steps. Sequential interval reductions from $\Delta S = .01$ to $\Delta S = .0001$ (based on $R = 1.0$) were employed in some cases.

The scaling relationship which exists for flat-faced slabs or cylinders serves an auxiliary purpose, namely, that of program checkout (excepting

those terms which vanish when $R \rightarrow \infty$). If the "two integration procedure" does not place the sonic point precisely at a chosen location, then an error exists in the program.

8.3 Nose Caps

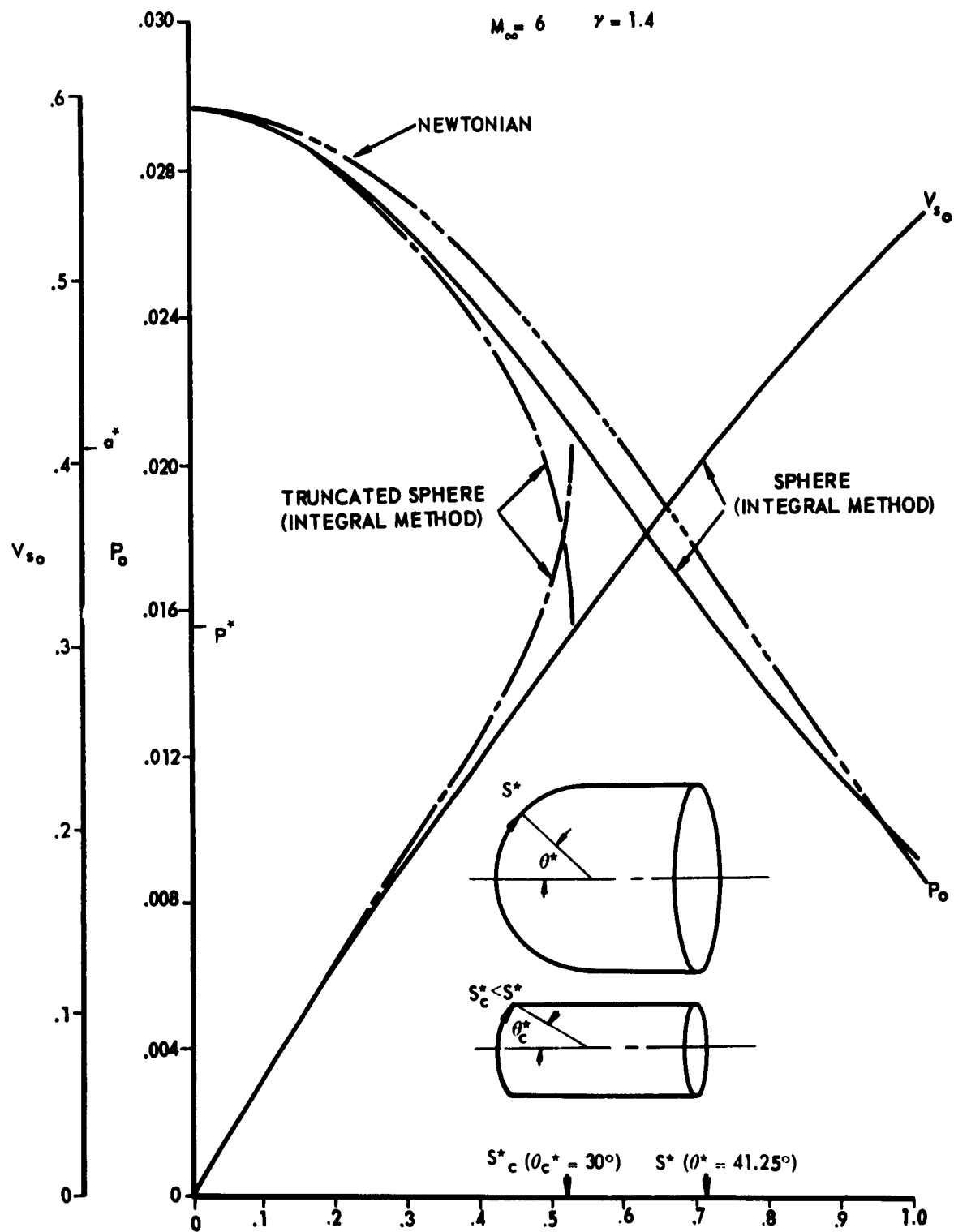
Having determined the flow field for a smooth nosed configuration, one may proceed to generate results for a family of nose "caps" provided that they terminate in a sonic corner. Modification of extrapolation procedures near the sonic point is necessary, however, to allow for the proper functional behavior in this neighborhood, e.g., infinite upstream U_{s_0} gradient.

The sphere provides a useful example for illustrating the preceding considerations. Representing the sphere shock standoff distance at a given M_∞ and γ by $\bar{\epsilon}$, each integration for a given $\epsilon < \bar{\epsilon}$ will produce results corresponding to a spherical cap. A few iterations are necessary in order to determine the value of ϵ corresponding to a specified corner location; however the convergence is relatively rapid. A comparison of results for complete and truncated spheres is shown in Fig. 28. The Newtonian value is also included for comparative purposes.

8.4 Two-Dimensional Results

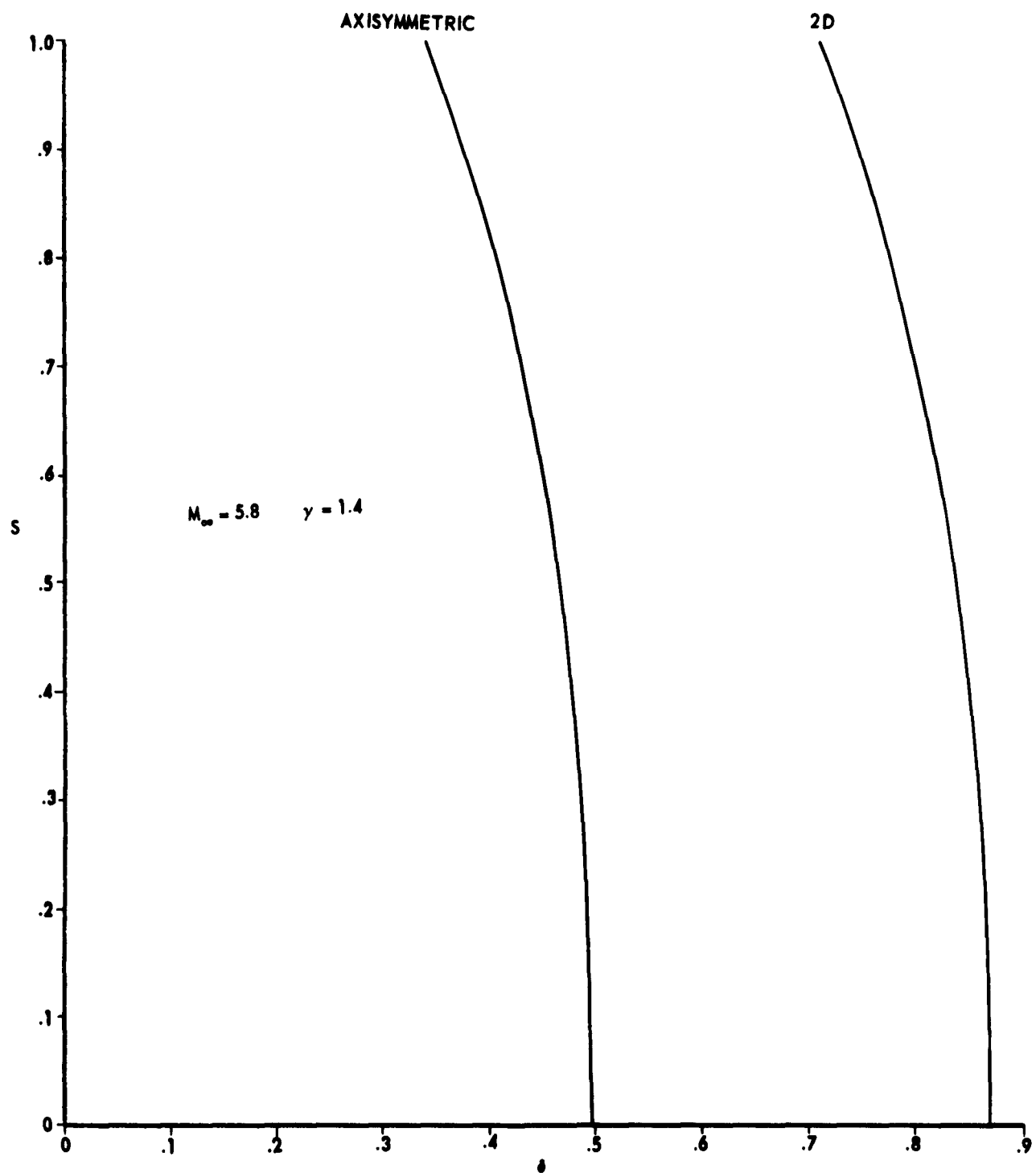
Flat-Faced Plate

Employing the step size reduction procedure used in the axisymmetric case near the corner, no difficulty was encountered in verifying the ϵ -scaling property for the two-dimensional flat-faced body, i.e., only two integrations were required to fix the sonic point precisely at the corner of the body. Figs. 29 and 30 give a comparison of shock shapes and surface pressure and velocity distributions for the flat-faced plate and cylinder. Referring to Eq. (3-2) for $R \rightarrow \infty$,



SURFACE PRESSURE AND VELOCITY DISTRIBUTIONS
FOR COMPLETE AND TRUNCATED SPHERES

FIGURE 28



SHOCK SHAPES - FLAT FACED PLATE AND CYLINDER

FIGURE 29

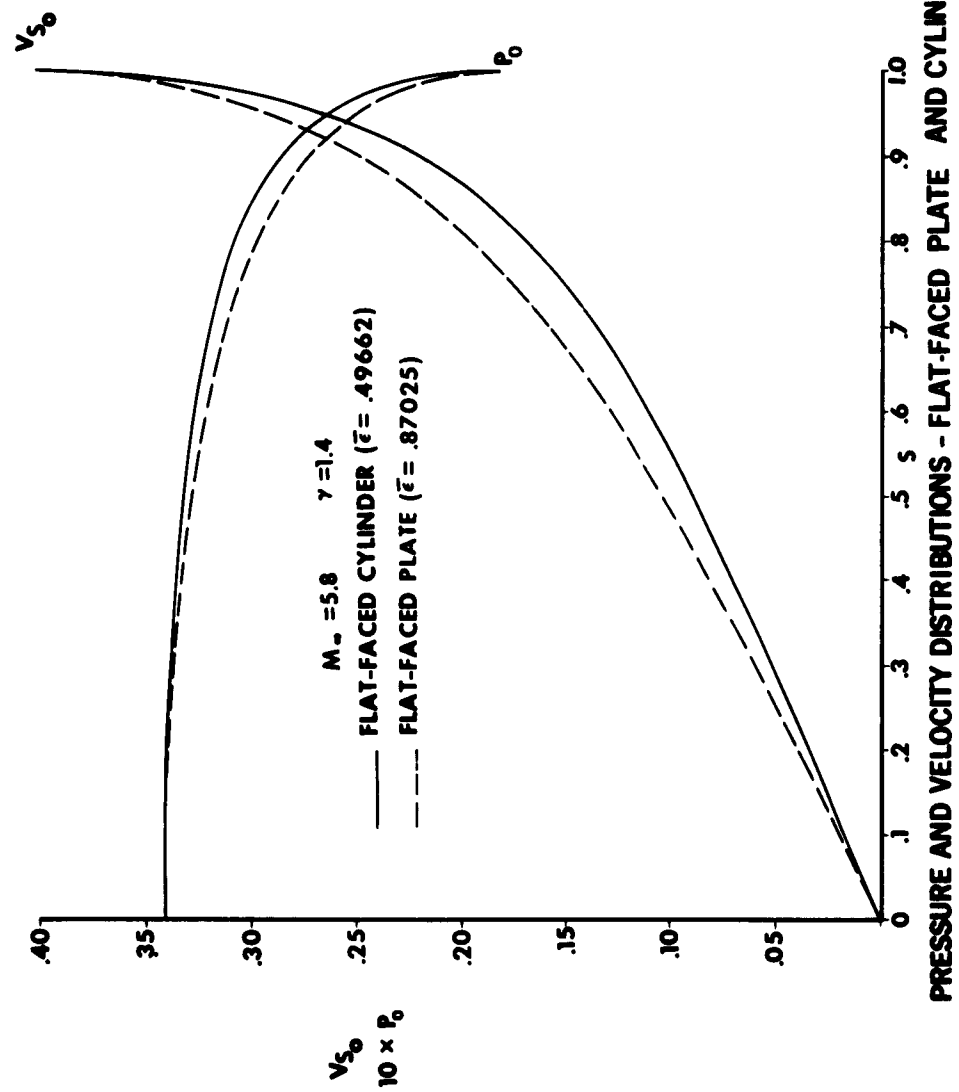


FIGURE 30

$$\left(\frac{dk}{ds}\right)_{2D} = \frac{2\bar{\epsilon}_{3D}}{\bar{\epsilon}_{2D}} \left(\frac{dk}{ds}\right)_{3D}$$

For $2\bar{\epsilon}_{3D} > \bar{\epsilon}_{2D}$, therefore, the shock curvature at the axis is greater for the axisymmetric case. This inequality was satisfied for the cases computed, e.g., for $M_\infty = 5.8$, $2(.49662) > .87025$.

Circular Cylinder

On the basis of preliminary evidence, the convergence procedure initially devised for the axisymmetric case was inadequate for handling two-dimensional bodies, i.e., circular cylinder.

The principal factor involved was the singular behavior of dk/ds for the same range of ϵ in which the velocity gradient displays erratic behavior. Setting tests which restricted shock curvature* (see Fig. 10) resulted in successful runs at discrete Mach numbers (e.g., $M_\infty = 4, 5$). However, the iteration displayed generally erratic and inconclusive behavior. For the converged runs, the shock wave displayed points of inflection in the supersonic regime which could not be ascribed to known physical behavior.

It is worth noting that the USSR cylinder results (Ref. 2) were presented primarily for the two and three strip calculations with only surface pressure data given for the one strip version (indicating the possibility of inadequacy of the one strip results). In addition, no other reference was found which presented two-dimensional integral method results of any description.

*For the axisymmetric case, Ref. 5 proposed a dk/ds test to handle situations where the initial ϵ guess is extremely poor.

9. CONCLUDING REMARKS

In the present report emphasis has been placed on the discussion of a representative formulation of the blunt body integral method which includes sufficient detail to delineate the numerical pitfalls involved as well as some practical limitations in its application. Particular importance was placed on the flow field determination in order to provide an accurate description of the flow properties across the shock layer. The gradient method was employed (for smooth bodies) since its application insured compatible tangential and normal flow property gradients at the shock and body while minimizing deviations in conservation of mass and momentum in the shock layer.

In the course of the investigation, a previously unreported feature of the method came to light, namely, that for the flat-faced cylinder case, the two point boundary value problem reduces to one involving a single integration of the system of governing equations. This feature obviously affords a significant reduction in computing time.

Regarding the practical utilization of the method, rational flow field data have been generated for a range of blunt-nosed axisymmetric configurations employing a combination of the integral method and the method of characteristics. Application of the latter method was found necessary in order to maintain downstream accuracy.

REFERENCES

1. Dorodnitsyn, A. A. "On a Method for Numerical Solution of Some Aero-Hydrodynamic Problems," Proc. Third All-Soviet Math. Congress, Vol. 2, 1956.
2. _____ "A Contribution to the Solution of Mixed Problems of Transonic Aerodynamics," Advances in Aeronautical Sciences, Vol. 2, Pergamon Press, 1959.
3. Belotserkovskii, O. M. "Flow Past a Circular Cylinder With a Detached Shock Wave," Dokl. Akad. Nauk, Vol. 113, No. 3, 1957.
4. _____ "On the Calculation of Flow Past Axisymmetric Bodies With Detached Shock Waves Using an Electronic Computing Machine," FMM, Vol. 24, No. 3, 1960.
5. Traugott, S. C. An Approximate Solution of the Supersonic Blunt Body Problem for Prescribed Axisymmetric Shapes. The Martin Company Research Report RR-13, August, 1958.
6. Vaglio-Laurin, R. "On the PLK Method and the Supersonic Blunt Body Problem," IAS Paper No. 61-22, January, 1961.
7. Holt, M, and G. H. Hoffman. "Calculation of Hypersonic Flow Past Spheres and Ellipsoids," IAS Paper No. 61-213-1907, June, 1961.
8. Gold, R., and M. Holt. Calculation of Supersonic Flow Past a Flat-Head Cylinder by Belotserkovskii's Method. Brown University, Div. of Appl. Math., AFOSR TN-59-199, March, 1959.
9. Holt, M. "Direct Calculation of Pressure Distribution on Blunt Hypersonic Nose Shapes With Sharp Corners," Journal of the Aerospace Sciences, Vol. 28., No. 11, November, 1961.
10. Feldman, S., and A. Widawsky. "Errors in Calculating Flow Fields by the Method of Characteristics," ARS Journal, Vol. 32, No. 3, March, 1962.
11. Kendall, J. M., Jr. Experiments on Supersonic Blunt Body Flows. Jet Propulsion Lab., C.I.T., Progress Report 20-372, Feb., 1959.
12. Sedney, R., and G. D. Kahl. Interferometric Study of the Blunt Body Problem. BRL Report No. 1100, April, 1960.
13. Hayes, W. D., and R. F. Probstein. Hypersonic Flow Theory. New York: Academic Press, 1959.
14. Gerber, N., and J. M. Bartos. Tables for Determination of Flow Variable Gradients Behind Curved Shock Waves. BRL Report No. 1086, Jan. 1960.

REFERENCES

15. Hakkinen, R. J. Supersonic Flow Near Two-Dimensional and Axially Symmetric Convex Corners and Curvature Discontinuities. Douglas Aircraft Company, Inc. Report No. SM-27747, July, 1958.
16. Friedman, M. P. "Two-Dimensional and Axisymmetric Rotational Flows Past a Transonic Corner," Journal of the Aerospace Sciences (Readers' Forum), Vol. 29, No. 4, April, 1962.
17. Belotserkovskii, O. M. Calculation of Flows Past Axially Symmetric Bodies With Detached Shock Waves (Computational Formulas and Tables of Flow Fields). Moscow: Computing Center, Academy of Sciences, 1961.

APPENDIX A

FLOW VARIABLE GRADIENTS AT SHOCK AND BODY

The governing equations expressed in body oriented curvilinear coordinates are given by

$$\frac{\partial}{\partial s}(\rho u_s r) + \frac{\partial}{\partial n}[(1 + \frac{n}{R})\rho u_n r] = 0 \quad (A1)$$

$$u_s \frac{\partial u_s}{\partial s} + (1 + \frac{n}{R})u_n \frac{\partial u_s}{\partial n} + \frac{u_s u_n}{R} + \frac{u_s}{\rho} \frac{\partial \rho}{\partial s} = 0 \quad (A2)$$

$$u_s \frac{\partial u_s}{\partial s} + (1 + \frac{n}{R})u_n \frac{\partial u_s}{\partial n} - \frac{u_s^2}{R} + \frac{u_s}{\rho} (1 + \frac{n}{R}) \frac{\partial \rho}{\partial n} = 0 \quad (A3)$$

$$u_s \frac{\partial}{\partial s}(\frac{\rho}{\rho^*}) + (1 + \frac{n}{R})u_n \frac{\partial}{\partial n}(\frac{\rho}{\rho^*}) = 0 \quad (A4)$$

Shock Gradients

The oblique shock equations serve as auxiliary relations in obtaining flow variable gradients immediately behind the shock wave. In addition, geometrical considerations (Fig. A1) enable one to express s -derivatives in terms of n - and k -derivatives, i.e., letting $\varphi = \frac{\pi}{2} - \theta - k$,

$$\left(\frac{d}{ds}\right)_s = \frac{dk}{ds} \frac{d}{dk} = \frac{\cos \varphi}{(1 + \frac{s}{R})} \left(\frac{\partial}{\partial s}\right)_s + \sin \varphi \left(\frac{\partial}{\partial n}\right)_s$$

or

$$\left(\frac{\partial}{\partial s}\right)_s = - \frac{(1 + \frac{s}{R})}{\cos \varphi} \left[\frac{1}{R_s} \frac{d}{dk} + \sin \varphi \left(\frac{\partial}{\partial n}\right)_s \right] \quad (A5)$$

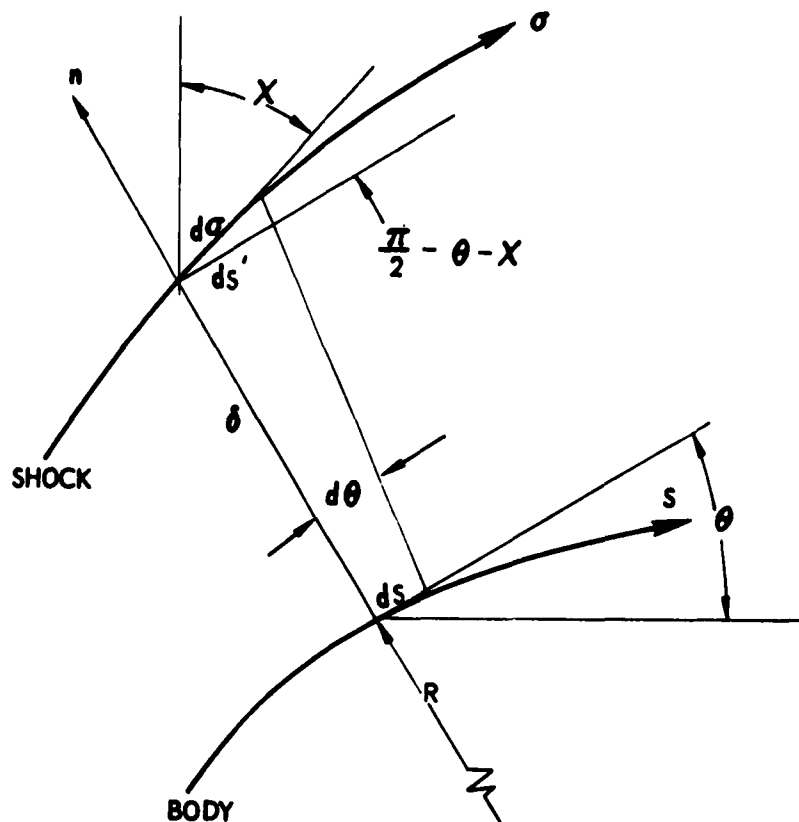


FIGURE A1

Use of this operator in Eqs. (A1), (A2), (A3) and (A4) results in an algebraic system of four equations for the gradients $(\partial p / \partial n)_s$, $(\partial p / \partial n)_s$, $(\partial \psi / \partial n)_s$, $(\partial \psi / \partial n)_s$. One subsequently obtains:

$$\left(\frac{\partial p}{\partial n}\right)_s = \frac{p_s}{k} \frac{[\tan \varphi \frac{f}{s} - g_s - \alpha_s / \beta_s]}{[\sec^2 \varphi - (\alpha_s / \beta_s)^2]} \quad (A6)$$

$$\left(\frac{\partial p}{\partial n}\right)_s = \frac{k}{\alpha_s^2} \left[\left(\frac{\partial p}{\partial n}\right)_s + \frac{\psi_s}{\alpha_s R_s \cos \varphi} \left(\frac{dp}{dk} - \frac{\alpha_s^2}{k} \frac{dp}{dk} \right) \right] \quad (A7)$$

$$\left(\frac{\partial \psi_s}{\partial n}\right)_s = \frac{1}{\alpha_s} \left[f_s - \frac{k \tan \varphi}{\rho_s} \left(\frac{\partial p}{\partial n}\right)_s \right] \quad (\text{A8})$$

$$\left(\frac{\partial \psi_s}{\partial n}\right)_s = \frac{1}{\alpha_s} \left[g_s + \frac{k}{\rho_s} \left(\frac{\partial p}{\partial n}\right)_s \right], \quad (\text{A9})$$

where

$$\alpha_s = \psi_s \tan \varphi - \psi_{ns}, \quad \alpha_s^2 = \frac{k \gamma \rho_s}{\rho_s}$$

$$f_s = \frac{-1}{R_s \cos \varphi} \left(\psi_s \frac{\partial \psi_s}{\partial r} + \frac{k}{\rho_s} \frac{\partial p}{\partial r} \right) + \frac{\psi_s \psi_{ns}}{R(1 + \frac{\gamma}{2})}$$

$$g_s = \frac{-1}{R_s \cos \varphi} \psi_s \frac{\partial \psi_s}{\partial r} - \frac{\psi_s^2}{R(1 + \frac{\gamma}{2})}, \quad R_s = \frac{-(1 + \frac{\gamma}{2})}{\frac{\partial \psi_s}{\partial r} \cos \varphi}$$

$$h_s = \frac{-1}{R_s \cos \varphi} \left(\frac{\partial \psi_s}{\partial r} + \frac{\psi_s}{r \rho_s} \frac{\partial p}{\partial r} \right) + \frac{\psi_{ns}}{R(1 + \frac{\gamma}{2})} + \frac{j}{r} (\psi_s \sin \theta + \psi_{ns} \cos \theta)$$

$$\frac{\partial p}{\partial r} = \frac{-4 \gamma M_\infty^2 (1 + \frac{\gamma-1}{2} M_\infty^2)^{-\frac{\gamma}{\gamma-1}} \sin \chi \cos \chi}{\gamma+1}$$

$$\frac{\partial p}{\partial r} = -4(\gamma+1) M_\infty^2 (1 + \frac{\gamma-1}{2} M_\infty^2)^{-\frac{\gamma}{\gamma-1}} \frac{\sin \chi \cos \chi}{[(\gamma-1) M_\infty^2 \cos^2 \chi + 2]^2}$$

$$\frac{d\psi_f}{df} = m \left[\frac{4}{f+1} \sin f \cos f \cos \theta + \frac{2}{f+1} \left(1 - 2 \sin^2 f - \frac{1}{M_\infty^2 \cos^2 f} \right) \sin \theta \right. \\ \left. - (\alpha \sin \theta - \beta \cos \theta) \frac{d\theta/ds}{df/ds} \right]$$

$$\frac{d\psi_h}{df} = m \left[\frac{-4}{f+1} \sin f \cos f \sin \theta + \frac{2}{f+1} \left(1 - 2 \sin^2 f - \frac{1}{M_\infty^2 \cos^2 f} \right) \cos \theta \right. \\ \left. - (\alpha \cos \theta + \beta \sin \theta) \frac{d\theta/ds}{df/ds} \right]$$

The data required to evaluate these gradients are M_∞ , f , θ , $\frac{d\psi}{ds}$, $\frac{d\theta}{ds}$, r , δ (note that $R_s = \frac{-(1+\delta/R)}{df/ds \cos \varphi}$ and $R = -\frac{1}{d\theta/ds}$).

One may now express the \mathcal{S} -derivatives in terms of the \mathcal{N} -derivatives through use of the original equations.

$$\left(\frac{\partial \psi}{\partial \mathcal{S}} \right)_f = -\frac{1}{\psi_f} \left[\left(1 + \frac{\delta}{R} \right) \psi_f \left(\frac{\partial \psi}{\partial \mathcal{N}} \right)_f - \frac{\psi_f^2}{R} + \frac{1}{\beta} \left(1 + \frac{\delta}{R} \right) \left(\frac{\partial \rho}{\partial \mathcal{N}} \right)_f \right] \quad (\text{A10})$$

$$\left(\frac{\partial \psi}{\partial \mathcal{S}} \right)_f = \frac{\psi_f}{\psi_f^2 - \alpha^2} \left\{ \frac{\alpha_f^2}{\psi_f} \left[\frac{\left(1 + \frac{\delta}{R} \right) \psi_f \left(\frac{\partial \rho}{\partial \mathcal{N}} \right)_f + \left(1 + \frac{\delta}{R} \right) \left(\frac{\partial \psi}{\partial \mathcal{N}} \right)_f}{\delta \beta} + \frac{\psi_f}{R} \right. \right. \\ \left. \left. + \frac{1}{\beta} \left(\psi_f \sin \theta + \left(1 + \frac{\delta}{R} \right) \psi_f \cos \theta \right) \right] - \left(1 + \frac{\delta}{R} \right) \psi_f \left(\frac{\partial \psi}{\partial \mathcal{N}} \right)_f - \frac{\psi_f \psi_{ff}}{R} \right\} \quad (\text{A11})$$

$$\left(\frac{\partial p}{\partial s}\right)_f = -\frac{\rho_f}{L} \left[\psi_f \left(\frac{\partial \psi_f}{\partial s}\right)_f + \left(1 + \frac{f}{R}\right) \psi_f \left(\frac{\partial \psi_f}{\partial n}\right)_f + \frac{\psi_f^2}{R} \right] \quad (A12)$$

$$\left(\frac{\partial p}{\partial s}\right)_f = -\frac{\rho_f}{L} \left\{ \left(1 + \frac{f}{R}\right) \psi_f \left(\frac{\partial p}{\partial n}\right)_f + \rho \left[\frac{1}{r_f} (\psi_f \sin \theta + \left[1 + \frac{f}{R}\right] \psi_f \cos \theta) \right. \right. \\ \left. \left. + \left(\frac{\partial \psi_f}{\partial s}\right)_f + \left(1 + \frac{f}{R}\right) \left(\frac{\partial \psi_f}{\partial n}\right)_f + \frac{\psi_f^2}{R} \right] \right\} \quad (A13)$$

[Alternative expressions may be determined through use of the equations $\rho_f \rho + V^2 = 1$ and $\rho_f r = f(M_\infty, \gamma, \gamma)$.]

Body Gradients

Expressions for $(\partial p / \partial n)_0$ and $(\partial \psi / \partial n)_0$ are obtained by setting $n=0$ and $\psi_0 = 0$ in the governing equations.

$$\left(\frac{\partial p}{\partial n}\right)_0 = \frac{\rho_0 \psi_0^2}{L R} \quad (A14)$$

$$\left(\frac{\partial \psi}{\partial n}\right)_0 = \left(\frac{\psi_0^2}{\alpha^2} - 1\right) \frac{d\psi_0}{ds} - \frac{1}{r_0} \psi_0 \sin \theta, \quad \alpha_0^2 = \frac{L \rho_0}{\rho} \quad (A15)$$

where $d\psi_0/ds$ is assumed known. Note that the coefficient of the surface velocity gradient vanishes at the sonic point indicating that similar behavior in the integral method is independent of the formulation and approximations employed.

The remaining normal derivatives are determined employing a procedure outlined in Ref. 15. Consider a function $f(\sigma, \tau)$ with $\sigma(\kappa, r)$ and $\tau(\kappa, r)$ defined as coordinates tangential and normal, respectively, to the streamline direction. One may therefore write

$$\frac{\partial f}{\partial \tau} = \frac{\partial f}{\partial r} \frac{dr}{d\tau} - \frac{\partial f}{\partial \sigma} \frac{d\sigma}{d\tau}$$

Assuming that $f = f(\tau; \kappa)$ (κ = shock wave angle at intersection of shock and streamline $\tau = \text{constant}$), the expression reduces to

$$\frac{\partial f}{\partial \tau} = \frac{\partial f}{\partial \kappa} \frac{d\kappa}{d\tau} \frac{dr}{d\tau}$$

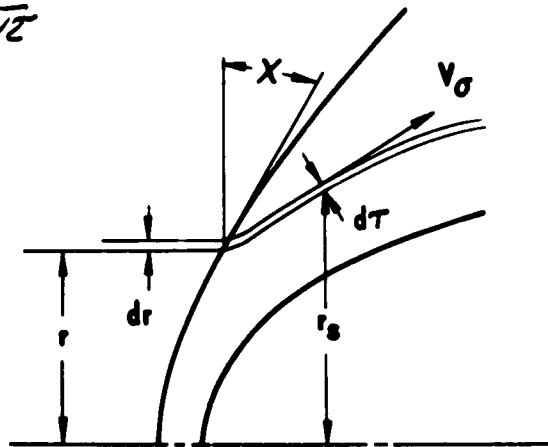


FIGURE A2

From continuity considerations

$$\left(\frac{\rho V}{\rho_\infty V_{\max}} \right) r dr = \rho u_\sigma r_s d\tau$$

or

$$\frac{dr}{d\tau} = \frac{\rho_\infty \rho u_\sigma r_s}{\rho}$$

$$C_{\infty} = \left[\frac{2}{(\gamma-1)M_{\infty}^2} \left(1 + \frac{\gamma-1}{2} M_{\infty}^2 \right)^{\frac{\gamma+1}{\gamma-1}} \right]^{\frac{1}{2}}$$

At the surface of the body, $\tau = 0$,

$$\left(\frac{\partial f}{\partial \tau} \right)_0 = \left(\frac{\partial f}{\partial n} \right)_0 = C_{\infty} \rho_0 \psi_0 r_0^j \left(\frac{\partial f}{\partial r} \right)_0 \left(\frac{1}{r_0} \frac{\partial f}{\partial f} \right)_0$$

Letting $\left(\frac{\partial f}{\partial r} \right)_0 = \frac{1}{R_0}$, $\left(\frac{R_0}{r} \right)_0 = (\cot f)_0$

$$\left(\frac{\partial f}{\partial n} \right)_0 = \frac{C_{\infty} \rho_0 \psi_0 r_0^j}{R_0^{1+j}} \left[(\cot f)_0^j \frac{\partial f}{\partial f} \right]_0$$

Setting $f = \frac{p}{\rho r}$

$$\frac{d(p/\rho r)}{df} = -\frac{p}{\rho r} \left[\frac{2\gamma \sin^2 f (M_{\infty}^2 \cos^2 f - 1)^2}{\left(\frac{2\gamma}{\gamma-1} M_{\infty}^2 \cos^2 f - 1 \right) \left(\frac{\gamma-1}{2} M_{\infty}^2 \cos^2 f + 1 \right) \cos f} \right]$$

Therefore

$$\left[\frac{\partial}{\partial n} \left(\frac{p}{\rho r} \right) \right]_0 = -j \frac{C_{\infty} \rho_0 \psi_0 r_0^j}{R_0^2} \left[\frac{2\gamma (M_{\infty}^2 - 1)^2}{\left(\frac{2\gamma}{\gamma-1} M_{\infty}^2 - 1 \right) \left(\frac{\gamma-1}{2} M_{\infty}^2 + 1 \right)} \right]_0 \frac{p_0}{\rho_0 r_0}$$

Finally

$$\left(\frac{\partial \rho}{\partial n}\right)_0 = \frac{\rho_0}{r_0} \left[\left(\frac{\partial \rho}{\partial n}\right)_0 - \rho_0 \left(\frac{\partial}{\partial n} \left[\frac{\rho}{\rho_0} \right] \right)_0 \right]$$

$$\left(\frac{\partial \psi}{\partial n}\right)_0 = \frac{1}{2\rho_0 r_0} \left[\rho_0 \left(\frac{\partial \rho}{\partial n}\right)_0 - \left(\frac{\partial \rho}{\partial n}\right)_0 \right]$$

The tangential derivatives at the surface are

$$\left(\frac{\partial \rho}{\partial s}\right)_0 = -\frac{\rho_0 r_0}{r_0} \frac{\partial \psi}{\partial s}$$

$$\left(\frac{\partial \rho}{\partial s}\right)_0 = -\frac{\rho_0}{r_0} \left[\frac{\partial \psi}{\partial s} + \left(\frac{\partial \psi}{\partial n}\right)_0 + \frac{1}{r_0} r_0 \sin \theta \right]$$

$$\left(\frac{\partial \psi}{\partial s}\right)_0 \equiv 0$$

$$\left(\frac{\partial \psi}{\partial s}\right)_0 \equiv \frac{\partial \psi}{\partial s}$$

Letting \mathcal{F} represent any flow variable, the angle between the curve $\mathcal{F} = \text{constant}$ and the x -axis is given by

$$\theta_{\mathcal{F}} = \theta + \tan^{-1} \left[-\left(\frac{\partial \mathcal{F}}{\partial s}\right) \left(\frac{\partial \mathcal{F}}{\partial n}\right) \right]$$

Hence, this angle may be determined at the shock and the body employing the derivatives given above.

APPENDIX B

BEHAVIOR OF THE SURFACE VELOCITY GRADIENT EXPRESSION IN THE NEIGHBORHOOD OF THE SONIC POINT

A computing scheme was devised which was intended to eliminate the need for curve fitting and extensive ϵ refinement required to cross the sonic point. It was based upon the following assumptions:

- a. Application of L'Hospital's rule to the equation for the surface velocity gradient yields a well behaved expression, exact at $S = S^*$ for $\epsilon = \bar{\epsilon}$.
- b. This expression approximates the correct value of dV_{so}/dS in some finite neighborhood of S^* overlapping the region in which the value calculated by the conventional expression is still valid.
- c. The expression is less sensitive to the initial value, ϵ , than the original gradient equation.

The scheme involved switching to the L'Hospital or "L" value just before dV_{so}/dS begins to behave erratically and switching back on the other side of the sonic point, e.g., Fig. B1.

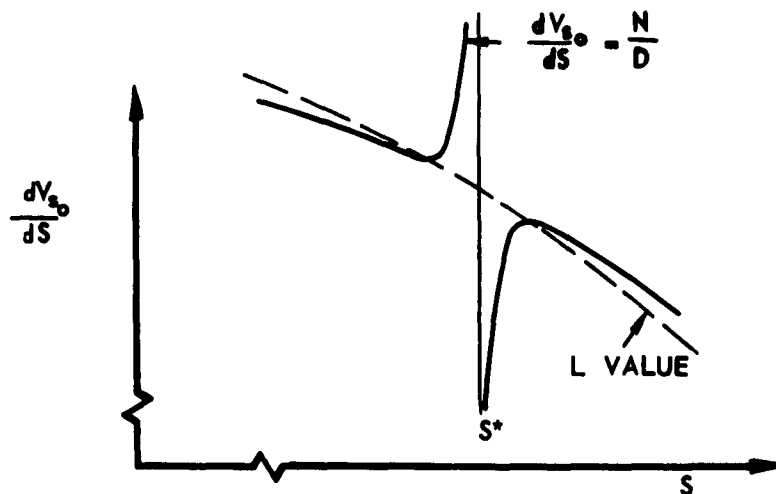


FIGURE B1

Switching expressions resulted in a temporary instability in the integration which recovered in the supersonic region. Characteristically, the integration process displayed strong "recovery" ability in that an erratic value introduced by stepping too close to ζ^* introduced only a temporary perturbation which was rapidly damped such that downstream results were relatively unaffected.

Mathematical Considerations

The denominator of the surface velocity gradient equation is given by

$$D = \frac{\zeta}{2} AB, \quad (B1)$$

where $A = (1 - \frac{\zeta+1}{\zeta-1} \zeta_0^2) = 0$ for $\zeta_0 = \zeta^* = (\frac{\zeta-1}{\zeta+1})^{\frac{1}{2}}$

$$B = (1 - \zeta_0^2)^{\frac{\zeta-1}{\zeta+1}} > 0 \text{ for } \zeta_0 < \zeta_{max} = 1$$

Now

$$\frac{dD}{d\zeta} = -\frac{\zeta}{2} \zeta_0 B \left[\frac{\zeta-1}{\zeta+1} A (1 - \zeta_0^2)^{-\frac{\zeta-1}{\zeta+1}} + \frac{\zeta+1}{\zeta-1} \right] \frac{d\zeta_0}{d\zeta} + \frac{\zeta}{2} B \left[\frac{\zeta-1}{\zeta+1} \frac{d\zeta_0}{d\zeta} + \zeta \sin \theta \right] \quad (B2)$$

Therefore

$$\lim_{\zeta \rightarrow \zeta^*} \frac{dD}{d\zeta} = -\zeta^* \left(\frac{2}{\zeta+1} \right)^{\frac{\zeta-1}{\zeta+1}} \left(\frac{\zeta+1}{\zeta-1} \right) \left(\frac{d\zeta_0}{d\zeta} \right)^* \quad (B3)$$

Assuming that the surface velocity gradient has a finite, nonzero value at $\zeta = \zeta^*$, the preceding considerations indicate that application of

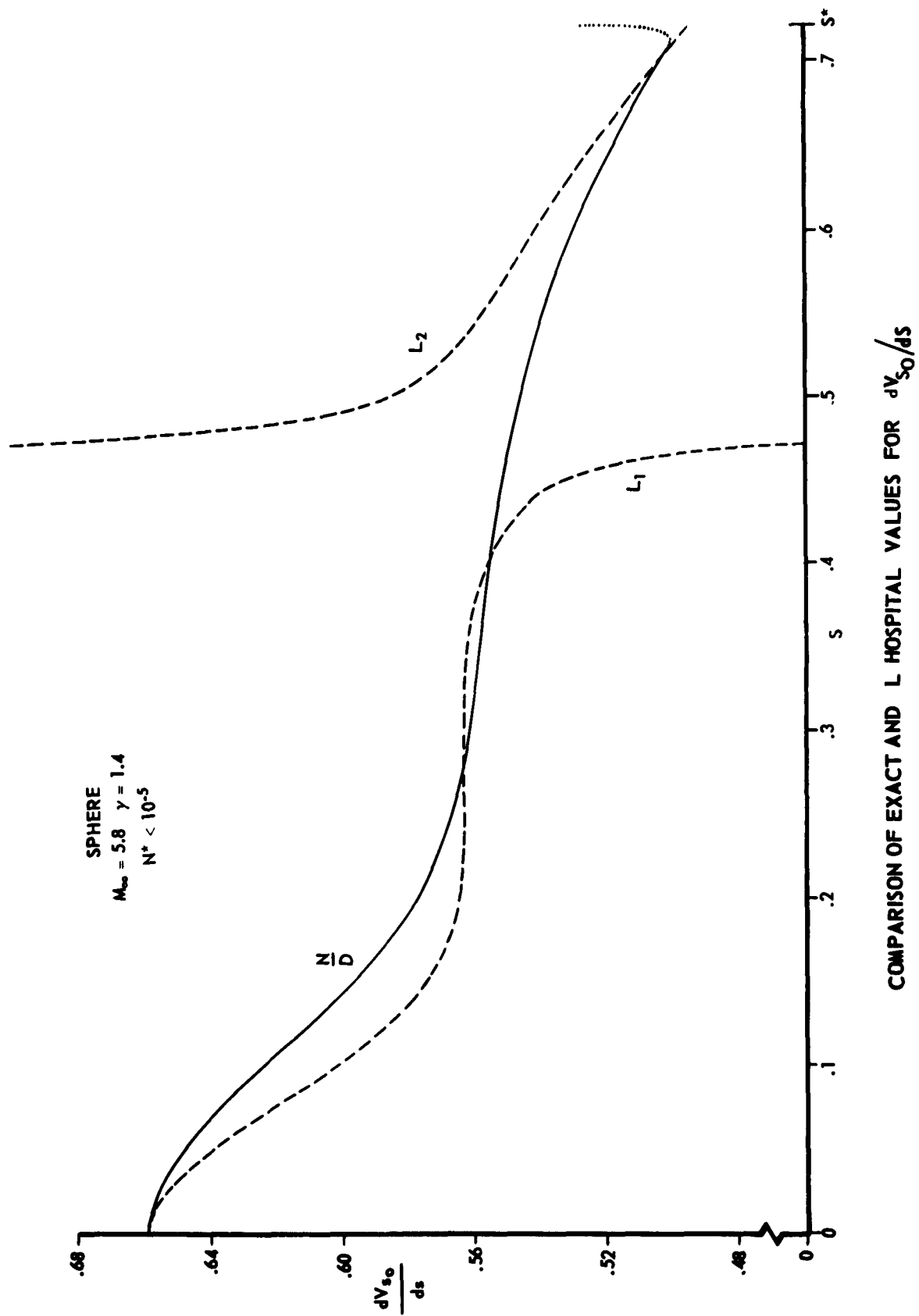


FIGURE B2

L'Hospital's rule yields an expression which is well behaved in the neighborhood of the sonic point. More explicitly,

$$\lim_{k_0 \rightarrow a^*} \frac{d\psi_0}{dS} = \lim_{k_0 \rightarrow a^*} \frac{\frac{dN}{dS}}{\frac{dD}{dS}} = \lim_{k_0 \rightarrow a^*} \left[\frac{\frac{\partial N}{\partial S} + \frac{\partial N}{\partial k_0} \frac{dk_0}{dS}}{\frac{\partial D}{\partial S} + \frac{\partial D}{\partial k_0} \frac{dk_0}{dS}} \right] \quad (B4)$$

$$\frac{d}{dS} = \frac{\partial}{\partial S} + \frac{dk_0}{dS} \frac{\partial}{\partial k_0} + \frac{dK}{dS} \frac{\partial}{\partial K}$$

Proceeding in an admittedly nonrigorous fashion, Eq. (B4) was treated as a quadratic expression for dk_0/dS (valid, hopefully, at $S=0$ and $S=S^*$). Subsequent evaluation of this expression indicated that one root gives the origin value correctly and the other root gives the sonic value correctly.

Carrying out the outlined scheme entailed a considerable amount of work in differentiating and expanding the N expression. Owing to its length (as well as its limited applicability) the resultant equation is not included here; however, a plot of the variation of the two roots \angle_1 and \angle_2 is given for a typical case, Fig. B2.

The proposed scheme was not adopted in view of the following considerations:

- a. The \angle_2 value did not approximate N/D with sufficient accuracy in a large enough neighborhood of the sonic point.
- b. The "switching transients" were more severe in some cases than erratic functional behavior due to stepping too close to S^* .

- c. The \angle value was sufficiently sensitive to the value of ϵ to require almost the same degree of ϵ refinement. This sensitivity is indicated in terms of dN/ds and dD/ds in Figs. B3 and B4, respectively. The practical advantage of utilizing the \angle expression is thus lost.
- d. The sheer bulk of the \angle expression contributed significantly to computing time expended.

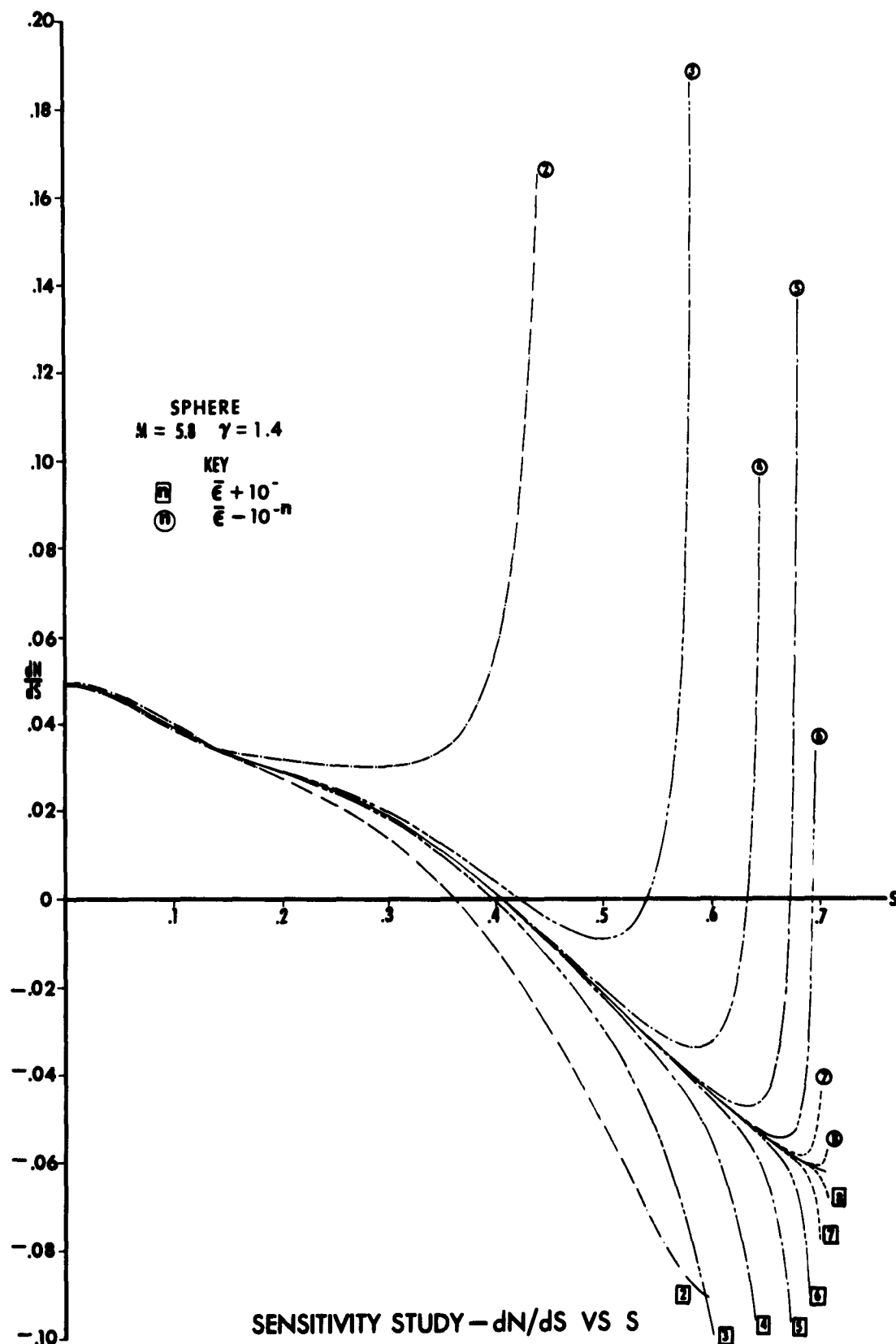


FIGURE B3

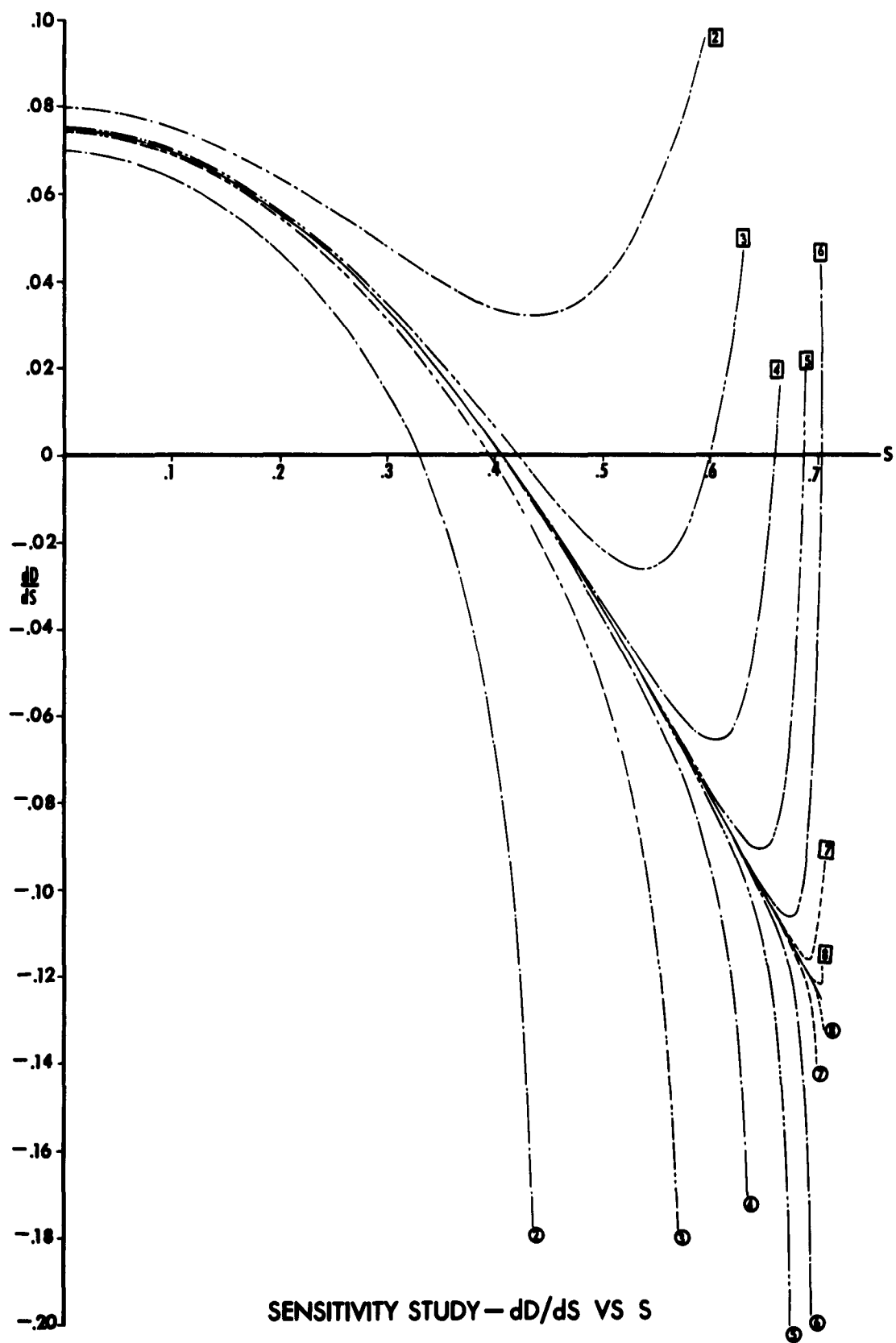


FIGURE B4